2024-02-07

# Complex erosional response to uplift and rock strength contrasts in transient river systems crossing an active normal fault revealed by 10Be and 26Al cosmogenic nuclide analyses

Boulton, S



10.1002/esp.5778
Earth Surface Processes and Landforms
Wiley

# Complex erosional response to uplift and rock strength contrasts in transient river systems crossing an active normal fault revealed by $^{10}$Be and $^{26}$Al cosmogenic nuclide analyses

Sarah J. Boulton[1*]; Ángel Rodés[2**], Derek Fabel[2], M. Cihat Alçiçek[3], Alexander C. Whittaker[4]

[1] School of Geography, Earth and Environmental Sciences, University of Plymouth, Drake's Circus, Plymouth, PL4 8AA, UK.

[2] Scottish Universities Environmental Research Centre, Scottish Enterprise Technology Park/Rankine Av, Glasgow G75 0QF, UK.

[3] Department of Geological Engineering, Pamukkale University, 20017 Denizli, Turkey.

[4] Department of Earth Science and Engineering, Royal School of Mines, Imperial College, London, SW7 2AZ, UK.

*Corresponding author:Sarah.boulton@plymouth.ac.uk

**Currently at Departamento de Xeografía, Universidade de Santiago de Compostela, Spain

## Abstract

Understanding the influence of bedrock lithology on the catchment-averaged erosion rates of normal fault-bounded catchments, and the effect that different bedrock erodibilties have on the evolution of transient fluvial geomorphology remain major challenges. To investigate this problem, we collected 18 samples for $^{10}$Be and $^{26}$Al cosmogenic nuclide analysis to determine catchment-averaged

erosion rates along the well-constrained Gediz Fault system in western Türkiye, which is experiencing fault-driven river incision owing to a linkage event ~ 0.8 Ma, and has weak rocks overlying strong rocks in the footwall. Combined with existing cosmogenic data, we show that the background rate of erosion of the pre-incision landscape can be constrained as < 92 $mMyr^{-1}$ and erosion rates within the transient reach vary from 16 – 1330 $mMyr^{-1}$. Erosion rates weakly scale with unit stream power, steepness index and slip rate on the bounding fault, although erosion rates are an order of magnitude lower than slip rates. However, there are no clear relationships between erosion rate and relief or catchment slope. Bedrock strength is assessed using Schmidt hammer rebound and Selby Rock Mass Strength Assessments; despite a 30-fold difference in erodibility there is no difference in the erosion rate between strong and weak rocks. We argue that for the Gediz Graben the strong lithological contrast effects the ability of the river to erode the bed resulting in a complex erosional response to uplift along the graben boundary fault. Weak co-variant trends between erosion rates and various topographic factors potentially result from incomplete sediment mixing or pre-existing topographic inheritance. These findings indicate that the erosional response to uplift along an active normal fault is a complex response to multiple drivers that vary spatially and temporally.

**Keywords**: Turkey, Türkiye, Active faulting, cosmogenic nuclides, rock strength, detachment-limited.

## 1. Introduction

The role of climate, tectonics and lithology on the evolution and form of bedrock (detachment-limited) streams is well known. The effect of tectonics, in particular the effect of variable uplift rates (i.e., Wobus et al., 2006; Kirby and Whipple, 2012; Whittaker, 2012; Whittaker and Boulton, 2012), and climate gradients (D'Arcy and Whittaker, 2014; Adams et al., 2020) on the rates and patterns of incision have been widely reported. Until recently the role of lithology and rock strength have attracted less attention and many studies have sought to remove or minimise this variable by choosing study areas with little rock variation (e.g. Miller et al., 2012; Ortega et al., 2013; Regalla et al., 2013; Snyder et al., 2000). However, landscape evolution modelling (Forte et al., 2016; 2020; Perne et al.,

2017, Darling et al., 2020; Mitchell and Yanites, 2021) and field investigations at the landscape (Bernard et al., 2019; Zondervan et al., 2020) and catchment scale (Sklar and Dietrich, 2001; Duvall, 2004; Whittaker et al., 2007; Kent et al., 2021; Gailleton et al., 2021; Peifer et al., 2021) have increasingly investigated the importance of lithology on river incision and fluvial geomorphology. Yet, there are still uncertainties in how bedrock properties influence catchment scale erosion, and how such characteristics can be effectively measured in the field.

Furthermore, while a number of studies have directly compared catchment-averaged erosion rates (CAER) to bedrock channel properties (i.e., Safran et al., 2005; Harkins et al., 2007; Ouimet et al., 2009; DiBiase et al., 2010; Cyr et al., 2010; Abbühl et al., 2011; Miller et al., 2013; Bellin et al., 2014; Kober et al., 2015). Relatively few studies have determined CAER along the strike of an active fault. For example Densmore et al. (2009) studied two faults in the western USA, the 18 km long Sweetwater fault and the 130 km Wassuk fault. Along neither fault were CAER found to be proportional to uplift rates nor to various topographic measures. Densmore et al. (2009) attributed the uncoupling of erosion from fault displacement to the influence of inherited high relief topography and the widespread occurrence of mass wasting. In contrast, Rossi et al. (2017) reported 26 erosion rates along a normal fault system in Baja California demonstrating a positive trend between CAER with slope and channel steepness. Roda-Boluda et al. (2019) also showed a linear relationship between CAER and the footwall component of fault throw rate from 15 samples taken from a series of catchments crossing an active normal fault system in southern Italy. In all these studies the footwalls of the studied faults are composed of metamorphic or igneous rocks with limited reported lithological variability at a regional scale.

This lithological homogeneity of existing research areas is significant, as the modelling of Forte et al. (2016) suggests that the presence of lithological contacts, where rock strength changes from strong to weak, will profoundly influence the response rates of an incising river system. For example, their modelling suggests that when soft rocks overlie hard rocks (along a contact dipping at 20 - 35° downstream) the lithological contact becomes an important and persistent topographic feature in the landscape. Interestingly, although the geological boundary moves downstream over time, the model suggests that erosion rates above and below the boundary should diverge. The soft rocks downstream erode

at the imposed uplift rate, but the underlying hard rocks erode at a rate lower than the regional uplift rate (Forte et al., 2016). The difference in the strength and bedrock erodibility between the hard and soft rocks controls the magnitude of difference between erosion and uplift rate, and also the duration of the landscape adjustment. Subsequent modelling studies by Perne et al. (2017), Darling et al. (2020), Wolpert and Forte (2021) and Mitchell and Yanites (2021) are broadly consistent with Forte et al. (2016)'s results. Although the more complex interbedded hard-soft rock scenarios of Darling et al. (2020)'s model indicate that in such cases the harder rocks may erode quicker than the soft rocks. A further implication of Forte et al.'s (2016) landscape evolution model is that CAER, determined from cosmogenic radionuclides (CRN - commonly $^{10}$Be), maybe affected by the relative enrichment of material from the harder rocks in the detrital sediment. Consequently, CAER would be perturbed or amplified because of the lithological variation.

Therefore, there is a knowledge gap in our understanding of how erosion rates change along faults with lithologically variable footwall geology. There is also the requirement to empirically test the results of models such as Forte et al. (2016), Perne et al. (2017) and Darling et al. (2020) in regions with complex geology to assess the applicability of these models to real systems.

Here, we use the well-constrained Gediz fault system (western Türkiye) as a natural laboratory to study the landscape response to fluvial incision across a strong lithological contrast (soft rocks over hard rocks) in the footwall of an active normal fault. As the geologic and geomorphic evolution of the region is well understood and constrained (i.e., Seyitoğlu and Scott, 1996; Seyitoğlu et al., 2002; Bozkurt, 2003; Bozkurt and Sözbilir, 2004; Çiftçi and Bozkurt, 2009a; Öner and Dilek, 2011; Kent et al., 2016; 2017; 2021), we can use the area to test the model predictions of Forte et al. (2016) and investigate the role that strength contrasts play in the evolution of transient landscape responses to base-level fall. This is achieved through a suite of new $^{10}$Be and $^{26}$Al CRN samples to determine CAER along the strike of the boundary faults combined with published cosmogenic data (Buscher et al., 2013; Heineke et al., 2019) and geomorphic indices (Kent et al., 2021). Catchment-averaged erosion rates are quantified using $^{10}$Be and $^{26}$Al so that the potential effect of sediment storage can be excluded, thus allowing

accurate exposure and denudation histories to be calculated (c.f., Bierman et al., 1999; Granger and Muzikar, 2001; von Blanckenburg, 2005).

## 2. Study area

The Gediz (also known as the Alaşehir) Graben is located in western Anatolia (Figure 1) forming an arcuate, asymmetric graben ~ 150 km in length. The Bozdağ Range to the south is uplifted along the southern graben-bounding normal fault and rises to over 2000 m in elevation. The ~ N-S extension forming this horst and graben structure has been ongoing since early Miocene times, probably as the result of roll-back along the Hellenic subduction zone (Okay and Satır, 2000; ten Veen et al., 2009) and can be divided into two main phases (Bozkurt and Sözbilir, 2004). Initial extension caused uplift along the now-inactive low-angle north-dipping Gediz detachment fault (Gessner et al., 2001; Seyitoğlu et al., 2002; Ring et al., 2003). The Gediz detachment fault presently dips to the N-NE at up to 32° and is gently corrugated along its strike (Sozbilir, 2012; Bozkurt and Sozbilir, 2012). The detachment forms the boundary between the Menderes Massif metamorphic rocks and overlying syn-tectonic sedimentary rocks (Figure 2). In the footwall, the Menderes Massif metamorphic core complex is composed mainly of Palaeozoic greenschist to amphibolite-facies schists, augengneisses, and paragneisses (Gessner et al., 2001; Ring et al., 2003).

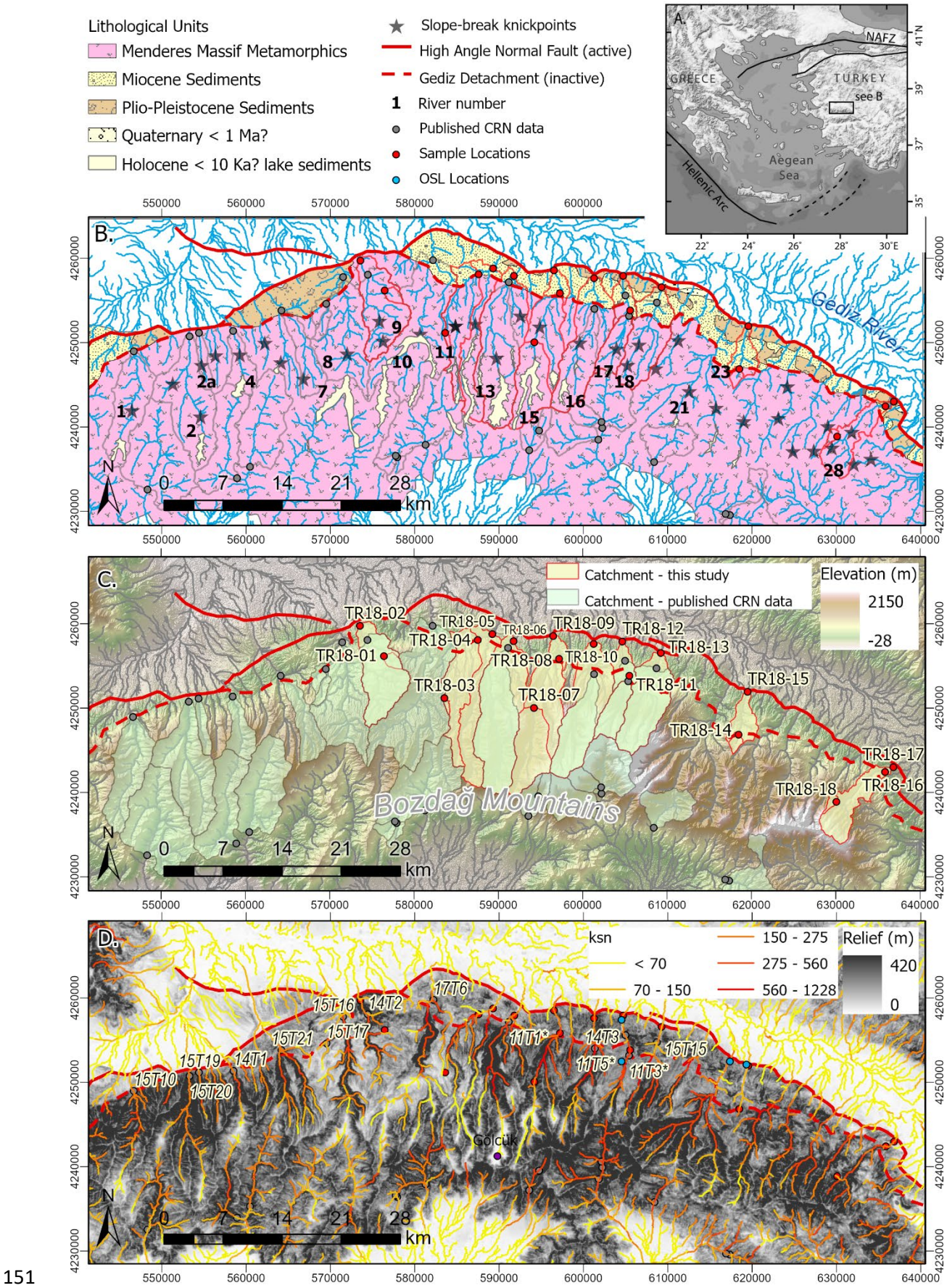
Lithological Units
Menderes Massif Metamorphics
Miocene Sediments
Plio-Pleistocene Sediments
Quaternary < 1 Ma?
Holocene < 10 Ka? lake sediments
Slope-break knickpoints
High Angle Normal Fault (active)
Gediz Detachment (inactive)
1 River number
Published CRN data
Sample Locations
OSL Locations
A.
NAFZ
GREECE
TURKEY
see B
Aegean Sea
Hellenic Arc
B.
Gediz River
C.
Catchment - this study
Catchment - published CRN data
Elevation (m)
2150
-28
TR18-01
TR18-02
TR18-03
TR18-04
TR18-05
TR18-06
TR18-07
TR18-08
TR18-09
TR18-10
TR18-11
TR18-12
TR18-13
TR18-14
TR18-15
TR18-16
TR18-17
TR18-18
Bozdağ Mountains
D.
ksn
< 70
70 - 150
150 - 275
275 - 560
560 - 1228
Relief (m)
420
0
Gölcük
0 7 14 21 28 km
N

*Figure 1A). regional location map showing the location of the Gediz Graben in Western Anatolia; B). geological map of the study area. Geological units are simplified from Kent et al. (2021) with additional mapping of Holocene lake deposits from Süzen et al. (2006). Numbers in bold indicate rivers sampled for CRN either in this study (table 1) or by Heineke et al. (2019) or Buscher et al. (2013) (table 3), rivers mentioned by name in the text are 9 - Akçapınar; 15 – Bozdağ; 16 - Gümüşcay; 17 - Kabazli; 21 – Kavaklidere; 23 – Yeniköy. Stars show location of slope-break knickpoints; C). topographic map of the study area (ALOS World 3D 30 m DEM) showing the sample locations with sample numbers collected during this study; D). relief map of the study are showing the steepnesss index of the rivers and the location of CRN samples collected by Buscher et al. (2013) indicated by * and Heineke et al. (2019) Also shown are the location of five OSL dates reported by Kent (2015) (unlabelled – blue) and the approximate location of the C14 date of Sullivan (1988) labelled as Gölcük. Following the cessation of slip on the Gediz detachment fault at ca. 2 Ma (Buscher et al., 2013), strain stepped northwards (basinwards) onto high angle faults. These include the presently active normal fault forming the range front fault (Figures 1 and 2) to the present-day topographic graben (Çifçi and Bozkurt, 2009a). In the uplifted footwall of the active fault are friable sedimentary rocks deposited originally on the hangingwall of the Gediz detachment. These sedimentary units, comprised mainly of early Miocene to Pliocene-aged alluvial fan and fluvial sandstones and conglomerates, unconformably overlie and derive from the metamorphic basement (e.g., Purvis and Robertson, 2004; 2005; Çiftçi and Bozkurt, 2009b).*

Quaternary sediments are variable in extent across the Bozdağ range (Figure 1). Fragments of river terraces have been reported by Kent (2015) along three rivers – the Yeniköy, Kavaklıdere and the Kabazlı (Figure 1B). These river terraces are of small spatial extent with OSL dates of five samples (Figure 1D) from the fine-grained facies of only one, well-developed, terrace level indicating aggradation between ~ 84 – 7.5 ka (Kent, 2015). However, in the headwaters of several of the larger river systems fluvial and lacustrine fine-grained sediments up to 170 m thick can be found (Süzen et al., 2006). Sediment cores from Gölcük Lake (Figure 1D) yielded $^{14}C$ dates of ≤ 10 ka (Sullivan, 1988) suggesting deposition during the Holocene to Pleistocene but ages of the older sediments are not constrained. These deposits are thought to have formed owing to 1 – 2° of rotation on the graben boundary fault during the Holocene resulting in slope reduction, lake formation, and sediment deposition (Süzen et al., 2006).

Across the Bozdağ Range, transverse bedrock rivers flow northwards into the Gediz Graben across the southern boundary fault. The rivers are generally deeply incised with prominent knickpoints and gorges upstream of the active fault. The slope-break knickpoints are not coincident with lithological boundaries (Kent et al., 2017) and are interpreted to mark the upstream extent of transient wave of river incision. Incision was caused by an increase in slip on the graben bounding fault as a result of the fault linkage of three initial fault segments ~ 0. 6 – 1 Ma (Kent et al., 2016; 2017). As a result of this linkage, present day throw rates (the vertical component of the slip rate) are now thought to be higher than the long-term average, with rates of up to 2 ± 0.2 $mmyr^{-1}$ calculated for the centre of the fault array (Kent et al., 2017).

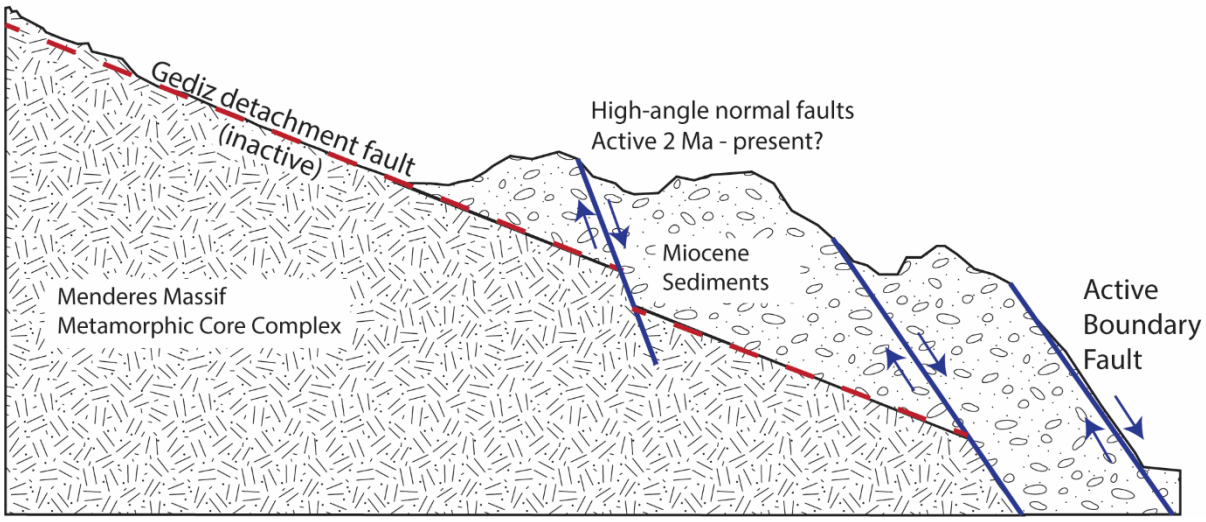


*Figure 2. Simplified cross-section of the northern margin of the Bozdağ Horst showing the relationship between low and high-angle faults (adapted from Kent et al., 2016).*

Kent et al. (2021) selected six of the transverse rivers to investigate the lithological controls on transient river behaviour. For simplicity, Kent et al. (2021) used two broad groupings of rock types; metamorphic and sedimentary in their quantitative analyses. Rivers were chosen to investigate differences in the proportion of metamorphic to sedimentary bedrock reaches (100% metamorphic in the Akçapınar River through to ~ 50% along the Yeniköy River; Figure 1B) and differences in uplift rate as a result of activity along the graben boundary fault. Here we continue to use these two broad lithologic groups to allow comparisons to this previous work.

# 3. Methods

## *3.1. Sample collection and CRN*

Eighteen samples of river sand from the active riverbed or sediment bars were collected from nine catchments draining northwards across the Gediz Graben boundary fault in May 2018 (Figures 1c and 3). The rivers were selected because either they had previously been sampled by Buscher et al. (2013) or were one of the six rivers studied in detail by Kent et al. (2021). Overall, a nested sampling strategy was adopted so that ten samples were collected from the range front where the rivers cross the active normal fault. On the easternmost river, two samples were collected ~ 2 km apart to assess downstream mixing and reproducibility. The remaining eight samples collected further upstream at either the lithological boundary between the sedimentary and metamorphic rocks or upstream of the knickpoint. Five of these eight samples were collected upstream of identified slope-break (tectonic) knickpoints identified by Kent et al. (2017) and the final three samples were collected at the low-angle detachment that forms the lithological boundary enabling comparison to published datasets. A further CRN dataset was published by Heineke et al. (2019) bringing the total number of samples analysed in the Gediz region to 33.

The eighteen samples collected here were sieved to 2 mm in field and further sieved to the 250-500 μm size fraction in the lab. Standard magnetic separation to concentrate the quartz fraction of the sample using a Franz magnetic separator was undertaken at the University of Plymouth. Subsequently samples were chemically leached using diluted HF, and between 16 and 20 grams of clean quartz cores were dissolved at SUERC together with ~0.29 grams of the CIAF-PH9 in-house $^{9}$Be carrier solution ([Be]=849 ± 12 ppm) following the procedure of Child et al. (2000). $^{10}$Be and $^{26}$Al concentrations were measured by the 5-MV NEC Pelletron accelerator mass spectrometer (AMS) at SUERC (Xu et al., 2010).

The results were input into the online CRONUS-Earth calculator v 3.0 (Balco et al., 2008) using the LSDn scaling, a sample density of 2.65 gcm$^{3}$ and NIST_27900 and Z92-0222 standardisations for $^{10}$Be and $^{26}$Al, respectively. Mean catchment elevation and shielding were derived from the ALOS World3D 30 m DEM, which has been shown to extract more accurate hydrological networks than other comparable global DEMs (Boulton and Stokes, 2018) using ArcGIS Pro 2.6.2 and TopoToolBox functions (Schwanghart and Scherler, 2014). Similarly, catchment

mean slope and relief over a 150 m radius were extracted using standard GIS tools.


*Figure 3 – Field photos showing landscapes and sampling in the Gediz region: A) View of the downstream reach of the Akçapınar River – a river characterised by 100% metamorphic bedrock, B) Sampling in the knickzone of the Bozdağ River, C) Sampling in the sedimentary reach of the Gümüşcay, note the well lithified Miocene clastic bedrock, D) Vertical step knickzone on the Kabazlı River at the boundary between the metamorphic basement and the sedimentary cover.*

Burial ages were derived from $^{10}$Be and $^{26}$Al data following the same principles as Granger and Muzikar (2001). This method allows solving of both the erosion rate corresponding to the initial $^{10}$Be and $^{26}$Al concentrations, and the average burial time after the exhumation of the quartz grains. To make them consistent with CRONUS v.3 results, scaled concentrations, spallation and muon production rates, and attenuation lengths were calculated as in Rodés (2021).

We also recalculated the $^{10}$Be sample concentrations reported in Buscher et al. (2013) and Heineke et al. (2019) for our study area using the same parameters stated above (e.g., using topographic shielding and a sample density of 2.65 gcm$^3$ and CRONUS v 3). Note that Heineke et al. (2019) did not apply a topographic shielding and used a sample density of 2.2 - 2.5 gcm$^3$ in addition to using v 2.3

of the CRONUS-Earth calculator, which results in differences in the erosion rates stated here compared to those reported in the original papers. Neither of these previous studies included $^{26}Al$ concentrations, so corrections for sediment reworking or burial cannot be determined for these previously published CRN data.

### *3.2. Sediment (un)mixing*

In the Bozdağ catchments studied samples were taken at the catchment outlet, at the major lithological boundary and in five locations above the slope-break knickpoint. This sampling strategy allows the erosion rates above (un-incised) and below (incised) the slope-break knickpoint to be deconvolved assuming that the same amount of quartz-bearing sediment is produced in both parts of the watershed. The sediment mixing is determined using the approach of Granger et al. (1996), as the CRN records the average erosion rate for the entire contributing catchment area. Therefore, the erosion rate between two sample points (a 'subcatchment') can be determined by correcting for the upstream sediment flux according to:

$$E_b = \frac{(E_c \times A_c) - (E_a \times A_a)}{A_b} \qquad \text{(e.q. 2)}$$

Where E ($mMyr^{-1}$) is the erosion rate of a catchment with area A ($m^2$), with subscripts indicting different subcatchments (Figure 4), where *c* is the entire catchment and *a* and *b* are the upstream and downstream subcatchments, respectively. In this study a *single* common value for the upstream erosion rate $E_A$ is used for all catchments owing to; a) the limited data on the CAER above the knickpoint, b) the assumption that this area represents a low relief and low erosion rate landscape formed prior to the uplift causing the present transient river incision.

ArcGIS Pro 2.6.2 was used to calculate the areas used in the unmixing calculations. The knickpoint finder tool in TopoToolBox (Schwanghart and Scherler, 2014; Stolle et al., 2019) was used to identify the highest knickpoint along all tributaries in the study area using a tolerance of 30. These were then used as pour points for the watershed tool, the results of which were then summed to determine the total unincised area in each river catchment, which is then

subtracted from the total catchment area calculated in the same way for the sample locations.

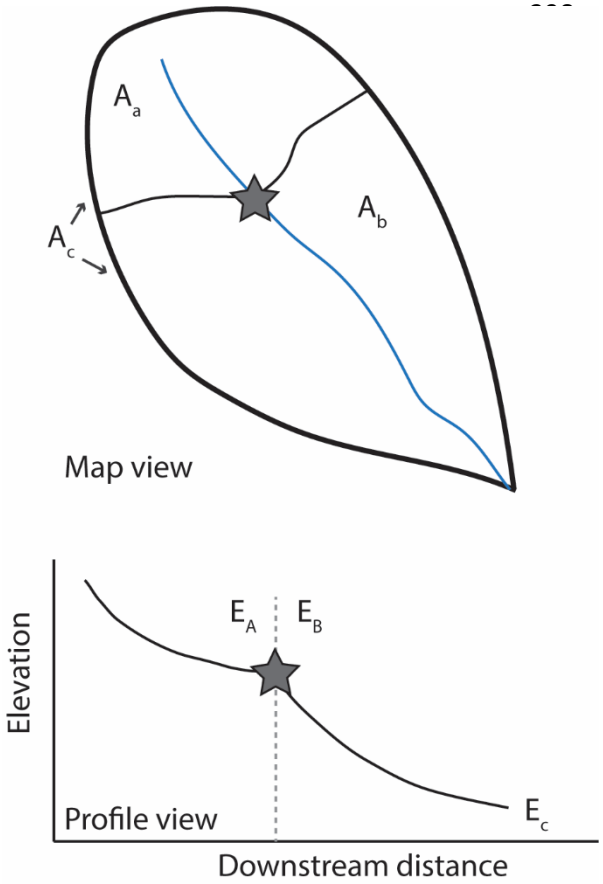


*Figure 4 – Conceptual diagram showing how different erosional zones add together to define total erosion rate at sample location. Top, a map view of a two zone mixing model showing the catchment areas above, Aa, and below, Ab, the knickpoint comprising the total catchment area Ac. Below, a topographic profile showing how the different zones relate to the transient river long profile with the samples collected at the knickpoint (star), EA, and at the river mouth, EC, allowing the determination of the erosion rate of only the transient, incising reach EB (modified from Rosenkranz et al. (2018).*

### *3.3. Calculation of unit stream power*

Geomorphic indices were calculated using ArcGIS Pro and TAK (Forte and Whipple, 2018), $k_{sn}$ values were determined with a $\Theta_{ref}$ = 0.45 following Kent et al (2017;2021) and the profiler function. While the choice of reference concavity can impact the resultant $K_{sn}$ values, Gailleton et al., (2021) demonstrated this is not significant.

Kent et al. (2021) constrained the rock strength (using Schmidt hammer rebound and Selby Rock Mass strength) and specific bedrock erodibility, *E*, using the unit stream power model (c.f., Whittaker et al., 2007; Attal et al., 2011; Zondervan et al., 2020):

$$E = k_b \omega = k_b \frac{\rho g Q S}{W} \quad \text{(e.q. 1)}$$

where the unit stream power, ω represents energy dissipation per unit channel area on the bed with units of $Wm^{-2}$, $\rho$ is the density of water, $g$ is the acceleration due to gravity, $Q$ is the water discharge ($m^3s^{-1}$), $S$ is local channel slope (m/m) and $W$ the channel width (m) as measured in the field. Consequently, specific bedrock erodibility, $k_b$, has units of $ms^2kg^{-1}$, representing the inverse of stress (c.f. Yanites et al., 2017).

Kent et al. (2021) demonstrate that the metamorphic rocks are around twice as hard as the sedimentary rocks. This difference is reflected by the bedrock erodibility, which was calculated as 2.2 - 6.3 x $10^{-14}$ $ms^2kg^{-1}$ in the metamorphic rocks. In contrast, bedrock erodibility values in the sedimentary units were 5 to 30 times larger (i.e., 5 to 30 times weaker) at 1.2 x $10^{-13}$ to 1.5 x $10^{-12}$ $ms^2kg^{-1}$ (Kent et al., 2021). Significantly, stream power was shown to scale with fault throw rate in the metamorphic rocks but not in the sedimentary units; potentially because the weaker sedimentary rocks themselves directly influence the fluvial processes and long-term erosional dynamics.

However, values for unit stream power (equation 3) for each river with reported CRN concentrations are required. Using the regional Q to A relationship determined using field measurements for the six rivers detailed in Kent et al. (2021), the estimate of Q for each river is found by extracting cumulative catchment area downstream along each sampled river at 100 m intervals using ArcGIS Pro 2.6.2 and the ALOS World 3D30 DEM. Similarly, the elevation is extracted at each point allowing the determination of local channel slope over each 100 m interval. The vertical accuracy of the AW3D30 DEM is < 5 m (Tadono et al., 2016). As field-derived measurements of width are not available for all rivers, width is calculated using the scaling relationships of Finnegan et al. (2005) and Whittaker et al. (2007) as well as using Kent et al.'s (2021) local hydraulic scaling relationship (see supplemental methods for more detail). These estimates of width are then used to derive the downstream distribution of unit stream power, ω, for each river. The maximum stream power was found for each river, and an average of the three stream powers taken. The error reported is the 2σ value on these values.

### *3.4. Rock strength and erodibility measurements*

*In situ* rock strength measurements can be used to estimate bedrock erodibility, which is related to the inverse of the lithologies tensile strength (Sklar and Dietrich, 2001). However, tensile strength measurements are difficult to measure in the field and as a result the Schmidt hammer is commonly utilised owing to the ease of use and portability (e.g., Goudie, 2016). Kent et al. (2021) used an N-type Schmidt hammer to characterise average bedrock uniaxial compressive strength for each lithological unit. Additionally, information on fracture characteristics was collected to calculate the semi-quantitative Selby Rock Mass strength – SRMS (Selby, 1980).

Twenty Schmidt hammer readings were taken at 130 locations along the six study rivers, the majority of which are from the metamorphic basement. At only eight locations could the Schmidt hammer reliably return a rebound value for the sedimentary rocks. At another 28 sites the exposed bedrock was too weak to accurately characterise the strength using this method and was recorded as having a rebound strength of < 20 (the effective limit of the Schmidt hammer), allowing the SRMS to be determined even where bedrock is very weak. Schmidt hammer rebound and SRMS are then averaged for the ~ 2 km upstream of the CRN sample locations where possible.

## 4. Results

### 4.1. $^{10}$Be and $^{26}$Al concentrations and catchment-wide erosion rate

The $^{10}$Be concentrations measured in the new samples range from 1.3 – 10.0 x $10^4$ atoms $g^{-1}$, while there were between 1.6 – 96.4 x $10^4$ atoms $g^{-1}$ of $^{26}$Al (Table 1). These values compare well to previously reported CRN concentrations of $^{10}$Be in the range 1.5 – 13.7 x $10^4$ atoms $g^{-1}$ (Supplemental Table 1) from sediment in rivers mainly draining the metamorphic basement (Buscher et al., 2013; Heineke et al., 2019).

*Table 1. New $^{10}$Be and $^{26}$Al analytical and derived erosion rate data with no corrections for subcatchments or sediment recycling/burial.*

| | Location | | | | | | | | | Measured concentrations* | | | | Denudation rates (no corrections)† | | | |
|---|---|---|---|---|---|---|---|---|---|---|---|---|---|---|---|---|---|
| Sample | Latitude (°N) | Longitude (°E) | River Name | River No (Kent) | Distance along strike (km) | Mean Catchment elevation (m)‡ | Topographic shielding | $^{10}$Be Production rate (at/g/yr) | $^{26}$Al Production rate (at/g/yr) | $^{10}$Be concentration (Atoms g$^{-1}$) | Uncertainty in $^{10}$Be concentration (Atoms g$^{-1}$) | $^{26}$Al concentration (Atoms g$^{-1}$) | Uncertainty in $^{26}$Al concentration (Atoms g$^{-1}$) | $^{10}$Be (m Myr$^{-1}$) | Internal uncertainty | $^{26}$Al (m Myr$^{-1}$) | Internal uncertainty |
| TR1801 | 38.44701 | 27.877054 | Akçapınar | 9 | 35.4 | 787 | 0.9898 | 7.6806 | 53.9639 | 19935 | 1483 | 107543 | 14843 | 236.0 | 17.6 | 316.0 | 43.6 |
| TR1802 | 38.48295 | 27.843433 | Akçapınar | 9 | 35.4 | 704 | 0.9750 | 7.0490 | 49.5853 | 29153 | 1527 | 207696 | 21774 | 150.0 | 7.9 | 150.0 | 15.8 |
| TR1803 | 38.4048 | 27.957544 | Sart Çay | 11 | 53.4 | 1002 | 0.9738 | 9.0573 | 63.4609 | 152808 | 4001 | 964210 | 51577 | 36.1 | 1.0 | 40.1 | 2.2 |
| TR1804 | 38.46693 | 28.003768 | Sart Çay | 11 | 53.4 | 844 | 0.9746 | 7.9411 | 55.7586 | 16803 | 1251 | 68007 | 9544 | 290.0 | 21.6 | 517.0 | 72.7 |
| TR1805 | 38.47295 | 28.024298 | Sart Çay | 11 | 53.4 | 854 | 0.9743 | 8.0088 | 56.2268 | 13521 | 1218 | 16163 | 6201 | 363.0 | 32.8 | 3060.0 | 1180.0 |
| TR1806 | 38.4651 | 28.052513 | Çaltili | 13 | 56.3 | 1018 | 0.9608 | 9.0620 | 63.4898 | 97728 | 3043 | 405368 | 27218 | 56.3 | 1.8 | 94.5 | 6.4 |
| TR1807 | 38.39361 | 28.079372 | Bozdağ | 15 | 60.3 | 1301 | 0.9663 | 11.4862 | 80.1738 | 92364 | 3127 | 531175 | 34773 | 72.9 | 2.5 | 88.3 | 5.8 |
| TR1808 | 38.4457 | 28.114133 | Bozdağ | 15 | 60.3 | 1215 | 0.9639 | 10.6928 | 74.7231 | 85558 | 2677 | 508773 | 33300 | 73.9 | 2.3 | 86.8 | 5.7 |
| TR1809 | 38.47007 | 28.106199 | Bozdağ | 15 | 60.3 | 1108 | 0.9640 | 9.8025 | 68.5974 | 74938 | 2245 | 462547 | 30666 | 78.1 | 2.4 | 88.6 | 5.9 |
| TR1810 | 38.46108 | 28.160952 | Gümüş Çayı | 16 | 65.4 | 1149 | 0.9594 | 10.0898 | 70.5714 | 26596 | 1521 | 124819 | 14650 | 222.0 | 12.7 | 339.0 | 39.9 |
| TR1811 | 38.42648 | 28.208946 | Kabazlı | 17 | 69 | 1347 | 0.9770 | 12.0506 | 84.0655 | 100108 | 3106 | 586261 | 36870 | 70.2 | 2.2 | 83.6 | 5.3 |
| TR1812 | 38.46332 | 28.200208 | Kabazlı | 17 | 69 | 997 | 0.9736 | 9.0205 | 63.2126 | 17481 | 1299 | 65090 | 9569 | 310.0 | 23.0 | 598.0 | 87.9 |
| TR1813 | 38.45042 | 28.252572 | Yeşilkavak | 18 | 73.7 | 983 | 0.9616 | 8.8043 | 61.7107 | 45207 | 1988 | 287656 | 20621 | 117.0 | 5.2 | 130.0 | 9.4 |
| TR1814 | 38.36203 | 28.356265 | Yeniköy | 23 | 85 | 795 | 0.9775 | 7.6208 | 53.5361 | 17675 | 1518 | 59004 | 8148 | 265.0 | 22.8 | 576.0 | 79.6 |
| TR1815 | 38.40754 | 28.369389 | Yeniköy | 23 | 85 | 526 | 0.9769 | 6.0361 | 42.5557 | 19759 | 1384 | 42834 | 7648 | 196.0 | 13.7 | 661.0 | 118.0 |
| TR1816 | 38.31973 | 28.553925 | Badınca | 28 | 105.1 | 1051 | 0.9574 | 9.2513 | 64.7776 | 38592 | 1806 | 300619 | 26206 | 142.0 | 6.7 | 129.0 | 11.3 |
| TR1817 | 38.32456 | 28.565227 | Badınca | 28 | 105.1 | 1034 | 0.9579 | 9.1283 | 63.9307 | 45977 | 2250 | 240144 | 19537 | 118.0 | 5.8 | 160.0 | 13.0 |
| TR1818 | 38.28846 | 28.487471 | Badınca | 28 | 105.1 | 1165 | 0.9642 | 10.2264 | 71.4968 | 22853 | 1559 | 153479 | 15142 | 262.0 | 17.9 | 277.0 | 27.4 |

* $^{10}$Be and $^{26}$Al concentrations were measured by the 5-MV NEC Pelletron accelerator mass spectrometer (AMS) at SUERC (Xu et al., 2010). Measured $^{10}$Be is normalised to the NIST_27900 st

† Denudation rates were calculated using the online CRONUS-Earth calculator v 3.0 (Balco et al., 2008) using the LSDn scaling and a sample density of 2.65 gcm$^{3}$.

‡ Sample elevation and shielding were derived from the ALOS World3D 30 m DEM

Therefore, apparent denudation rates range between 36 to 363 mMyr$^{-1}$ and 40 to 3060 mMyr$^{-1}$ for $^{10}$Be and $^{26}$Al, respectively. However, the denudation rates estimated from both nuclides agree within error for < 30% of the samples. These samples show $^{26}$Al/$^{10}$Be ratios in the range 6.2 – 7.8. The samples with a larger deviation between the derived denudation rates of each nuclide have significantly depleted $^{26}$Al/$^{10}$Be ratios of < 5.2 (Table 2). In a two-isotope diagram (Figure 5), 44% of data points cluster in the 0 – 0.5 Ma burial zone; 17% in the 0.5 – 1 Ma burial zone and 39% of points in the > 1 Ma burial zone. These data indicate that a simple exposure/denudation history, without taking into account sediment storage, is incorrect for the majority of samples and implies that sediment reworking from the alluvial plain and/or the uplifted sediments is contributing a significant component of the transported bedload in many rivers (c.f. Granger et al., 1996).

*Table 2.* $^{26}Al/^{10}Be$ ratios, *burial age and recalculated total catchment erosion rates based upon burial corrections.*

| Sample name | $^{26}Al/^{10}Be$ ratio | Burial age (Ma) | Burial corrected erosion rate (m/Myr) |
|---|---|---|---|
| TR1801 | 5.4±0.9 | 0.60 ± 0.41 | 174 ± 45 |
| TR1802 | 7.1±0.8 | 0.00 ± 0.34 | 149 ± 19 |
| TR1803 | 6.3±0.4 | 0.21 ± 0.25 | 32 ± 5 |
| TR1804 | 4.0±0.6 | 1.19 ± 0.41 | 159 ± 42 |
| TR1805 | 1.2±0.5 | 4.40 ± 1.03 | 40 ± 19 |
| TR1806 | 4.1±0.3 | 1.05 ± 0.27 | 33 ± 6 |
| TR1807 | 5.7±0.4 | 0.39 ± 0.27 | 60 ± 11 |
| TR1808 | 5.9±0.4 | 0.33 ± 0.27 | 63 ± 11 |
| TR1809 | 6.2±0.5 | 0.26 ± 0.27 | 69 ± 12 |
| TR1810 | 4.7±0.6 | 0.87 ± 0.36 | 144 ± 33 |
| TR1811 | 5.9±0.4 | 0.36 ± 0.26 | 59 ± 10 |
| TR1812 | 3.7±0.6 | 1.35 ± 0.43 | 157 ± 42 |
| TR1813 | 6.4±0.5 | 0.22 ± 0.28 | 105 ± 20 |
| TR1814 | 3.3±0.5 | 1.60 ± 0.42 | 119 ± 33 |
| TR1815 | 2.2±0.4 | 2.49 ± 0.48 | 56 ± 16 |
| TR1816 | 7.8±0.8 | 0.00 ± 0.18 | 139 ± 10 |
| TR1817 | 5.2±0.5 | 0.62 ± 0.30 | 86 ± 17 |
| TR1818 | 6.7±0.8 | 0.12 ± 0.34 | 248 ± 45 |

Therefore, the $^{26}Al$ data allows the calculation of an average burial history and the determination of a new erosion rate taking into account the depletion of the $^{10}Be$ and $^{26}Al$ concentration during the time that the quartz grains were buried (Table 2). This calculation gives 'burial-corrected' erosion rates of 32 to 248 $mMyr^{-1}$ for the study area catchments. Unfortunately, a similar calculation cannot be undertaken on the existing published CRN datasets (Buscher et al., 2013; Heineke et al., 2019) as there are no reported $^{26}Al$ data. As these sites are predominantly located in the footwall of the detachment fault, where there is little or no outcrop of sediments, it suggests that sediment storage should be limited for these samples. However, the presence of Holocene or older sediments in some catchments is a source of potential error that cannot be accounted for in the previously published data, and may explain why the published erosion rates are in general slightly higher than those reported here. This hypothesis is supported by the $^{26}Al/^{10}Be$ ratios of three of samples upstream of the boundary between the sedimentary rocks and the Menderes Massif metamorphics falling in the > 1 Ma burial zone (Figure 5).

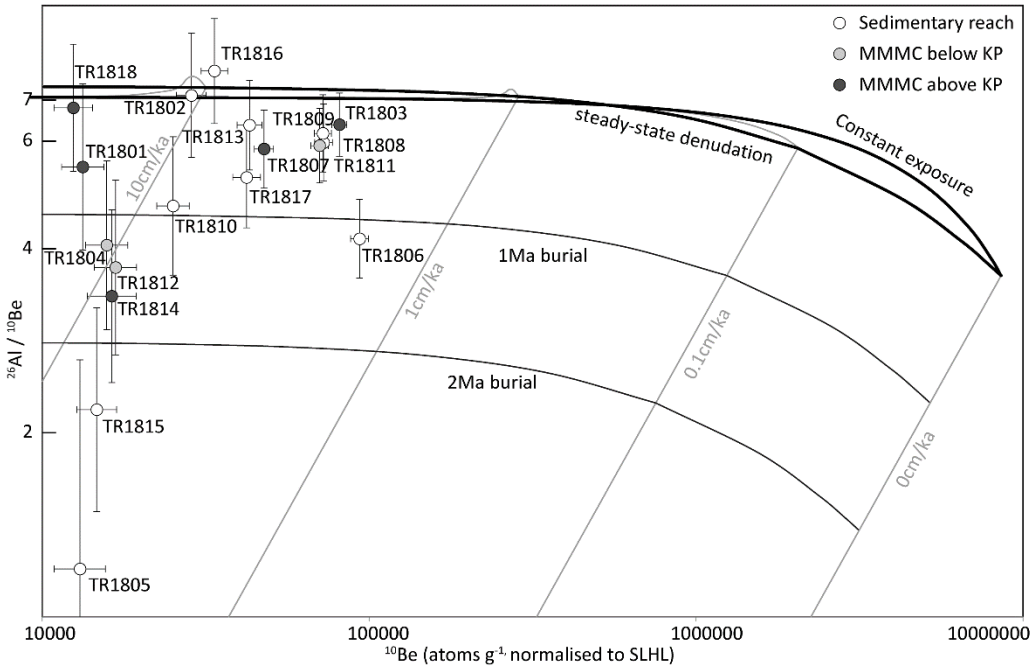


*Figure 5. $^{26}Al/^{10}Be$ vs $^{10}Be$ ratio two isotope diagram showing burial model and concentration data scaled to surface production rates (Lal, 1991) for measured samples. Surface muon contributions of 0.99±0.20% and 1.45±0.29% were considered for $^{10}Be$ and $^{26}Al$ respectively. Samples taken above the slope-break knickpoint are indicted by the grey symbols. MMMC = Menderes Massif Metamorphic core complex. Error bars include analytical and production rate uncertainties.*

On five rivers, samples were taken at or upstream of the slope-break knickpoint (TR18-01; 03; 07; 14; 18). These samples represent the denudation rate prior to landscape rejuvenation and transient river incision, as a result of fault linkage ~ 0.8 Ma (Kent et al., 2017), providing constraints for the unmixing model to determine the rate of erosion excluding these low erosion rate areas. Samples TR18-03 and TR18-07 give the lowest burial-corrected erosion rates at 32 and 60 $mMyr^{-1}$, respectively. Ridge crest erosion rates determined by Heineke et al. (2019) also fall in the range ~ 30 – 90 $mMyr^{-1}$. Whereas, samples TR18-01 and TR18-18 give much higher rates of 174 and 248 $mMyr^{-1}$, respectively; while TR18-14 returns an intermediate value of 119 $mMyr^{-1}$. Significantly, these latter three samples have only small catchment areas upstream of the sample point (1.7 - 3 $km^2$), which may be below a threshold for an appropriate size of catchment area. Additionally, the CAER from $^{10}Be$ and $^{26}Al$ nuclides are not within error and

consequently indicate variable sediment recycling, which is difficult explain in the metamorphic headwaters. Therefore, given the higher values than for the ridge crests, small catchment areas and incomplete mixing, these latter three samples are not used to determine the erosion rate upstream of the knickpoint. Instead, the average of the other two samples is taken to be representative of the low incision zone and used for all catchments (c.f., Roda-Boluda et al., 2018). Therefore, the average CAER used is 46 $mMyr^{-1}$ above the knickpoints.

### *4.2. Results from unmixing model*

In a landscape experiencing transient river incision, erosion rates above the knickpoint are expected to be lower than below the knickpoint. Therefore, we used a unmixing method (e.g., Granger et al., 1996; Rosenkranz et al., 2018) to remove the influence of such low erosion rates on downstream samples. Using the minimum erosion rate estimate determined above (i.e. 46 $mMyr^{-1}$), it is possible to derive a quantitative estimate for the erosion rates within the transient reach; i.e., upstream of the active fault and downstream of the knickpoint. This method is applied to both the new burial-corrected CAER and also the previously published CRN datasets (Table 3). The effect of applying this unmixing model is variable depending on the proportion of the total catchment area falling in the low erosion rate zone above the knickpoint, and on the difference between the low erosion rate and the denudation rate determined for the downstream sample (Table 3). For example, where the downstream initial burial-corrected CAER are relatively low (such as on the Bozdağ) the unmixing results in a small increase in CAER (e.g., from 63 $mMyr^{-1}$ to 99 $mMyr^{-1}$). But where the difference between the assumed upstream erosion rate of 46 $mMyr^{-1}$ and the downstream sample is greater, the final calculated rate is markedly higher. For example, on the Gumuşçay the initial burial-corrected CAER is 144 $mMyr^{-1}$, which increases to 1330 $mMyr^{-1}$ after unmixing; a tenfold increase. For the majority of samples the rates do increase, but a limited number of samples from or close to the lithological boundary result in no or negligible change. This is because the measured rate is close to the low erosion rate value even though the samples are within the knickzone. For one sample - 14T1 (Heineke et al., 2019), this adjustment results in a negative erosion rate. This CAER is not included in further analyses.

*Table 3. Parameters used in the unmixing calculations to remove effect of low erosion rate and resultant erosion rates (Eb) for transient reach.*

| Sample No | River No | Catchment area ($m^2$) Aa | Ab | Ac | Erosion rates (LSDn)(m/Myr) Ea | ± | Ec | ± | Eb | ± |
|---|---|---|---|---|---|---|---|---|---|---|
| 15T10 | 1 | 23827405 | 19380606 | 43208011 | 46 | 14 | 55 | 7 | 65 | 23 |
| 15T20 | 2 | 33018658 | 30633406 | 63652064 | 46 | 14 | 46 | 6 | 45 | 20 |
| 15T19 | 2a | 3713634 | 3729325 | 7442959 | 46 | 14 | 82 | 11 | 118 | 26 |
| 14T1 | 4 | 12346068 | 4072945 | 16419013 | 46 | 14 | 33 | 4 | -6 | 45 |
| 15T21 | 7 | 5464432 | 16719167 | 22183599 | 46 | 14 | 79 | 10 | 90 | 14 |
| 15T16 | 8 | 37403840 | 26672597 | 64076437 | 46 | 14 | 92 | 14 | 157 | 39 |
| 15T17 | 8 | 3186523 | 815578.2 | 4002101 | 46 | 14 | 73 | 10 | 180 | 73 |
| TR18-02 | 9 | 25649691 | 20803431 | 46453122 | 46 | 14 | 149 | 19 | 276 | 46 |
| 14T2 | 9 | 25649691 | 20803431 | 46453122 | 46 | 14 | 187 | 37 | 361 | 84 |
| 17T6 | 10 | 68662720 | 27467993 | 96130713 | 46 | 14 | 250 | 39 | 760 | 141 |
| TR18-05 | 11 | 43799839 | 26295684 | 70095523 | 46 | 14 | 40 | 19 | 30 | 56 |
| TR18-04 | 11 | 43799839 | 26295684 | 70095523 | 46 | 14 | 159 | 42 | 347 | 114 |
| 11T1* | 13 | 45492741 | 35010065 | 80502806 | 46 | 14 | 60 | 7 | 77 | 24 |
| TR18-06 | 13 | 45492741 | 35010065 | 80502806 | 46 | 14 | 33 | 6 | 16 | 23 |
| TR18-09 | 15 | 47765237 | 22648803 | 70414040 | 46 | 14 | 69 | 12 | 118 | 48 |
| TR18-08 | 15 | 47765237 | 22648803 | 70414040 | 46 | 14 | 63 | 11 | 99 | 45 |
| TR18-10 | 16 | 30641229 | 5400620 | 59651748 | 46 | 14 | 144 | 33 | 1330 | 373 |
| 11T5* | 16 | 30641229 | 5400620 | 36041849 | 46 | 14 | 61 | 6 | 148 | 89 |
| TR18-12 | 17 | 11032158 | 16141920 | 27174078 | 46 | 14 | 157 | 42 | 233 | 71 |
| 14T3 | 17 | 11032158 | 11455766 | 22487924 | 46 | 14 | 151 | 22 | 252 | 45 |
| TR18-11 | 17 | 11032158 | 5741419 | 16773577 | 46 | 14 | 157 | 10 | 370 | 40 |
| 11T3* | 17 | 11032158 | 5558898 | 16591056 | 46 | 14 | 63 | 8 | 95 | 37 |
| TR18-13 | 18 | 13303890 | 32870296 | 46174186 | 46 | 14 | 105 | 20 | 129 | 29 |
| 15T15 | 18 | 13303890 | 32870296 | 46174186 | 46 | 14 | 239 | 43 | 317 | 61 |
| 11T4* | 18 | 13303890 | 13624552 | 26928442 | 46 | 14 | 126 | 17 | 204 | 36 |
| TR18-15 | 23 | 1932233 | 12999221 | 14931454 | 46 | 14 | 56 | 16 | 57 | 18 |
| TR18-17 | 28 | 15970937 | 12825476 | 28796413 | 46 | 14 | 86 | 17 | 136 | 42 |
| TR18-16 | 28 | 15970937 | 12219002 | 28189939 | 46 | 14 | 139 | 10 | 261 | 29 |

## *4.3. Relationship between CAER and geomorphic indices*

These calculations enable the comparison between erosion rates to a number of geomorphic and geologic measures (Table 4). The burial-corrected mixed rates (i.e., CAER for the entire catchment) and the burial-corrected unmixed rates for the transient reaches (with the area upstream of the knickpoint removed) are compared alongside the recalculated published CAER (Buscher et al., 2013;

Heineke et al., 2019) and the published CAER unmixed for the low erosion rate area, to investigate the relationships between different factors and erosion along the southern margin of the Gediz Graben.

| River Name | River No (Kent) | Sample | $^{10}$Be source | Distance along strike (km) | Catchment area (km$^2$) | Mean catchment slope (°) | Mean slope above KP (°) | Mean slope below KP (°) | Mean catchment relief (m) | Mean catchment relief above KP (m) | Mean catchment relief below KP (m) | $k_{sn}$ upstream of sample ($m^{0.9}$) | error | Maximum stream power ($Wm^{-2}$) | error | Max incision upstream of sample (m) | Throw rate @fault since 0.7 Ma ($mmyr^{-1}$) | Long term throw rate since 2 Ma ($mmyr^{-1}$) |
|---|---|---|---|---|---|---|---|---|---|---|---|---|---|---|---|---|---|---|
| Akçapınar | 9 | TR1801 | This study | 35.4 | 3 | 12.6 | 15.16 | 20.85 | 60 | 66 | 101 | 184.4 | 2.7 | 1987 | 2314 | 132 | 1.41 | 0.44 |
| Akçapınar | 9 | TR1802 | This study | 35.4 | 46 | 16.7 | 15.16 | 20.85 | 78 | 66 | 101 | 69.7 | 1.4 | 1987 | 406 | 356 | 1.41 | 0.44 |
| Sart Çay | 11 | TR1803 | This study | 53.4 | 1 | 8.8 | 15.17 | 18.47 | 77 | 66 | 85 | 161.3 | 2.5 | 1792 | 2080 | 29 | 1.84 | 0.99 |
| Sart Çay | 11 | TR1804 | This study | 53.4 | 5 | 17.5 | 15.17 | 18.47 | 77 | 66 | 85 | 94.4 | 2.0 | 1792 | 528 | 209 | 1.84 | 0.99 |
| Sart Çay | 11 | TR1805 | This study | 53.4 | 38 | 17.5 | 15.6 | 18.47 | 79 | 66 | 85 | 94.4 | 2.0 | 1792 | 528 | 308 | 1.84 | 0.99 |
| Çaltili | 13 | TR1806 | This study | 56.3 | 80 | 20.5 | 18.33 | 24.49 | 102 | 90 | 124 | 107.8 | 2.6 | 2600 | 704 | 615 | 1.91 | 1.28 |
| Bozdağ | 15 | TR1807 | This study | 60.3 | 34 | 20.3 | 18.33 | 22.02 | 96 | 90 | 107 | 70.0 | 0.8 | 6163 | 427 | 564 | 2 | 1.42 |
| Bozdağ | 15 | TR1808 | This study | 60.3 | 64 | 21.5 | 18.33 | 22.02 | 101 | 90 | 107 | 91.7 | 0.7 | 6163 | 818 | 564 | 2 | 1.42 |
| Bozdağ | 15 | TR1809 | This study | 60.3 | 70 | 19.3 | 18.33 | 22.02 | 99 | 90 | 107 | 100.3 | 3.3 | 6163 | 1198 | 564 | 2 | 1.42 |
| Gümüş Çayı | 16 | TR1810 | This study | 65.4 | 60 | 21.7 | 22.41 | 20.75 | 106 | 112 | 100 | 123.7 | 3.2 | 3986 | 1060 | 634 | 1.86 | 1.33 |
| Kabazlı | 17 | TR1811 | This study | 69 | 17 | 24.7 | 18.97 | 17.33 | 84 | 92 | 81 | 133.7 | 2.7 | 2376 | 1454 | 279 | 1.74 | 1.33 |
| Kabazlı | 17 | TR1812 | This study | 69 | 28 | 17.6 | 18.97 | 17.33 | 84 | 92 | 81 | 104.3 | 2.2 | 2376 | 1439 | 331 | 1.74 | 1.33 |
| Yeşilkavak | 18 | TR1813 | This study | 73.7 | 46 | 21.1 | 23.75 | 19.81 | 101 | 117 | 95 | 133.7 | 2.7 | 3274 | 1454 | 355 | 1.58 | 1.48 |
| Yeniköy | 23 | TR1814 | This study | 85 | 3 | 16.7 | 18.28 | 16.34 | 88 | 88 | 78 | 161.3 | 2.5 | 1046 | 2080 | 211 | 1.3 | 0.99 |
| Yeniköy | 23 | TR1815 | This study | 85 | 15 | 18.4 | 18.28 | 16.34 | 80 | 88 | 78 | 75.8 | 1.8 | 1046 | 2628 | 240 | 1.3 | 0.99 |
| Badınca | 28 | TR1816 | This study | 105.1 | 2 | 23 | 24.97 | 19.4 | 111 | 125 | 93 | 45.0 | 1.9 | 2144 | 1060 | 442 | 0.72 | 0.59 |
| Badınca | 28 | TR1817 | This study | 105.1 | 28 | 23 | 24.97 | 19.4 | 110 | 125 | 93 | 123.7 | 3.2 | 2144 | 1060 | 442 | 0.72 | 0.59 |
| Badınca | 28 | TR1818 | This study | 105.1 | 29 | 21.5 | 24.97 | 19.4 | 105 | 125 | 93 | 38.1 | 1.8 | 2144 | 1416 | 300 | 0.72 | 0.59 |
| Çay Sokak | 10 | 17T6 | Heineke et al. (2019) | 44.6 | 157 | 16 | 14.82 | 17.39 | 72 | 69 | 83 | 142.3 | 1.0 | 3838 | 1416 | 418 | 1.65 | 0.87 |
| Armutlu | 1 | 15T10 | Heineke et al. (2019) | 5.6 | 70 | 21.9 | 14.85 | 26.27 | 101 | 71 | 132 | 142.3 | 1.0 | 930 | 1416 | 722 | 0.7 | 0.7 |
| Yeşilkavak | 18 | 15T15 | Heineke et al. (2019) | 73.7 | 3 | 22.1 | 23.75 | 19.81 | 102 | 117 | 95 | 104.3 | 2.2 | 3274 | 1439 | 355 | 1.58 | 1.48 |
| Başiktaş Der | 8 | 15T16 | Heineke et al. (2019) | 32.9 | 104 | 16 | 15.17 | 16.41 | 73 | 66 | 78 | 26.2 | 0.8 | 1203 | 4343 | 372 | 1.35 | 0.9 |
| Başiktaş Der | 8 | 15T17 | Heineke et al. (2019) | 32.9 | 7 | 9.4 | 15.17 | 12.81 | 73 | 66 | 78 | 165.5 | 5.4 | 548 | 4343 | 70 | 1.35 | 0.9 |
| Kazımpaşa | 2a | 15T19 | Heineke et al. (2019) | 13.65 | 12 | 25.5 | 15.16 | 25.63 | 122 | 116 | 127 | 165.5 | 5.4 | 1192 | 4343 | 286 | 0.87 | 0.59 |
| Yenikuruder | 2 | 15T20 | Heineke et al. (2019) | 12.8 | 104 | 24.2 | 19.06 | 27.03 | 114 | 93 | 137 | 75.8 | 1.8 | 1023 | 2628 | 760 | 0.87 | 0.59 |
| Irlamaz Çayi | 7 | 15T21 | Heineke et al. (2019) | 22.7 | 36 | 21.7 | 15.17 | 23.02 | 98 | 77 | 111 | 133.7 | 2.7 | 1539 | 1454 | 289 | 1.1 | 0.71 |
| Cevizdere | 4 | 14T1 | Heineke et al. (2019) | 17.7 | 28 | 22.4 | 18.09 | 24.52 | 107 | 101 | 122 | 133.7 | 2.7 | 1998 | 1454 | 533 | 0.99 | 0.81 |
| Akçapınar | 9 | 14T2 | Heineke et al. (2019) | 35.4 | 69 | 17.1 | 15.16 | 20.85 | 76 | 66 | 101 | 161.3 | 2.5 | 1987 | 2080 | 356 | 1.41 | 0.44 |
| Kabazlı | 17 | 14T3 | Heineke et al. (2019) | 69 | 1 | 24.7 | 18.97 | 17.33 | 82 | 92 | 81 | 84.7 | 2.0 | 2376 | 631 | 331 | 1.74 | 1.33 |
| Çaltili | 13 | 11T1* | Buscher et al. (2013) | 56.3 | 80 | 21.5 | 18.33 | 24.49 | 103 | 90 | 124 | 58.0 | 1.0 | 2600 | 631 | 615 | 1.91 | 1.28 |
| Kabazlı | 17 | 11T3* | Buscher et al. (2013) | 69 | 28 | 18.6 | 18.97 | 17.33 | 84 | 92 | 81 | 138.8 | 0.7 | 2141 | 1282 | 279 | 1.74 | 1.33 |
| Yeşilkavak | 18 | 11T4* | Buscher et al. (2013) | 73.7 | 42 | 24.9 | 23.75 | 17.33 | 102 | 117 | 95 | 138.8 | 0.7 | 3274 | 1282 | 355 | 1.58 | 1.48 |
| Gümüş Çayı | 16 | 11T5* | Buscher et al. (2013) | 65.4 | 59 | 24.7 | 22.41 | 19.81 | 116 | 112 | 100 | 80.5 | 1.7 | 3986 | 1282 | 634 | 1.86 | 1.33 |

*Table 4. Geomorphic and geological variables by sample and river.*

Firstly, if the along strike geomorphic character of the uplifted footwall of the Gediz Graben boundary fault is examined, it is clear that the mean catchment relief (Figure 6A), maximum incision (Figure 6B) and mean catchment slopes (Figure 6C) of sampled catchments are variable (Figure 6B) but overall follow the trend in fault throw rate (Figure 6B) with minima all metrics coinciding with the mapped fault segment boundaries (dashed lines, Figure 6). Indeed, the clear relationship along strike of the geomorphic expression of active faulting was partly used by Kent et al. (2016) to determine long-term uplift rates along the Gediz Graben boundary fault (Figure 6B). If the relief (Figure 6A) and slope (Figure 6C) above and below the knickpoints are considered separately, the same overall trends are apparent but with higher relief and slopes downstream of the knickpoint in the central and western parts of the range. This result is expected as the transient wave of incision causes gorge formation and hillslope steepening as it propagates through the river system. In the eastern part of the range this relationship is apparently inverted with higher slopes and relief above the knickpoint. Although, fewer data are available in this zone.

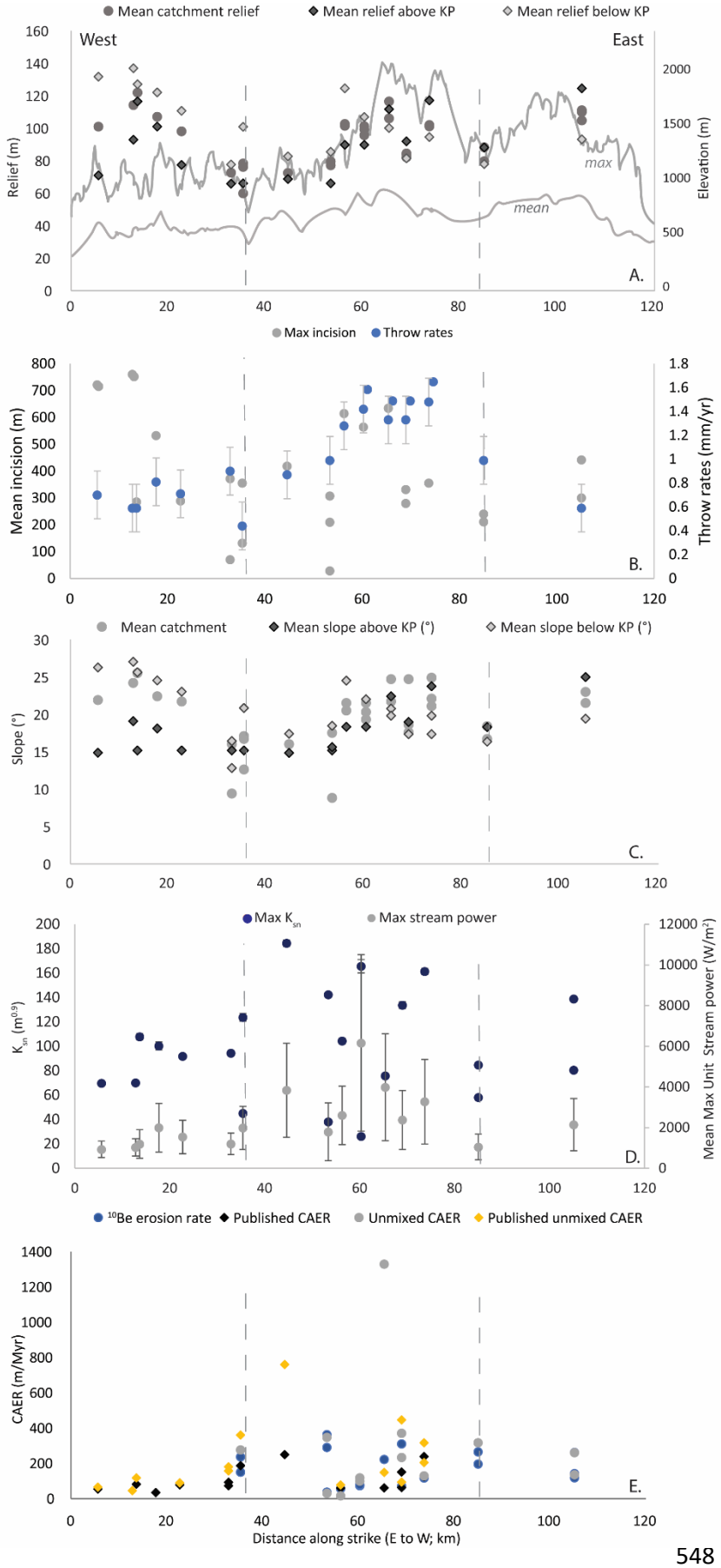


*Figure 6. Along strike trends in geomorphic variables and CAERs. Dashed lines show fault segment boundaries from Kent et al. (2018). A) Catchment relief (mean whole catchment, mean above and below the tectonic knickpoint, and elevation mean and maximum swath profiles; B) Channel incision in the transient reaches and long-term throw rates (Kent et al., 2017);C)Total mean catchment slope and mean slope above and below the knickpoint; D) Normalised steepness index and maximum unit stream power, and E) Catchment-averaged erosion rates. Note: error bars are shown where greater than symbol size.*

When the normalised steepness index in the transient reach is plotted along strike then the highest steepness indices are present in the centre of the fault array (Figure 6D), where current fault slip rates are highest. Maximum stream powers also cluster within the central fault segment, although it is important to acknowledge that lower values of steepness index and stream power are also present in the central part of the fault zone.

When the along strike trends in CAER are considered there is an increase from the westernmost sample (54.5 $mMyr^{-1}$) into the centre of the range (250 $mMyr^{-1}$) for both the raw CAER and burial-corrected rates (Figures 6E and 7). However, rates then decrease again along two large river systems in the centre of the range (TR18-06 – Catili and TR18-09 – Bozdaĝ) before increasing again along the eastern part of the range. This decrease in erosion rates in the centre of the fault appears unexpected given these catchments are experiencing the highest uplift rates. When the unmixed CAER are plotted (Figure 6E), a clearer pattern of lower rates at the fault tips and higher rates in the centre of the range appears although the CAER in the centre of the fault are still generally subdued.

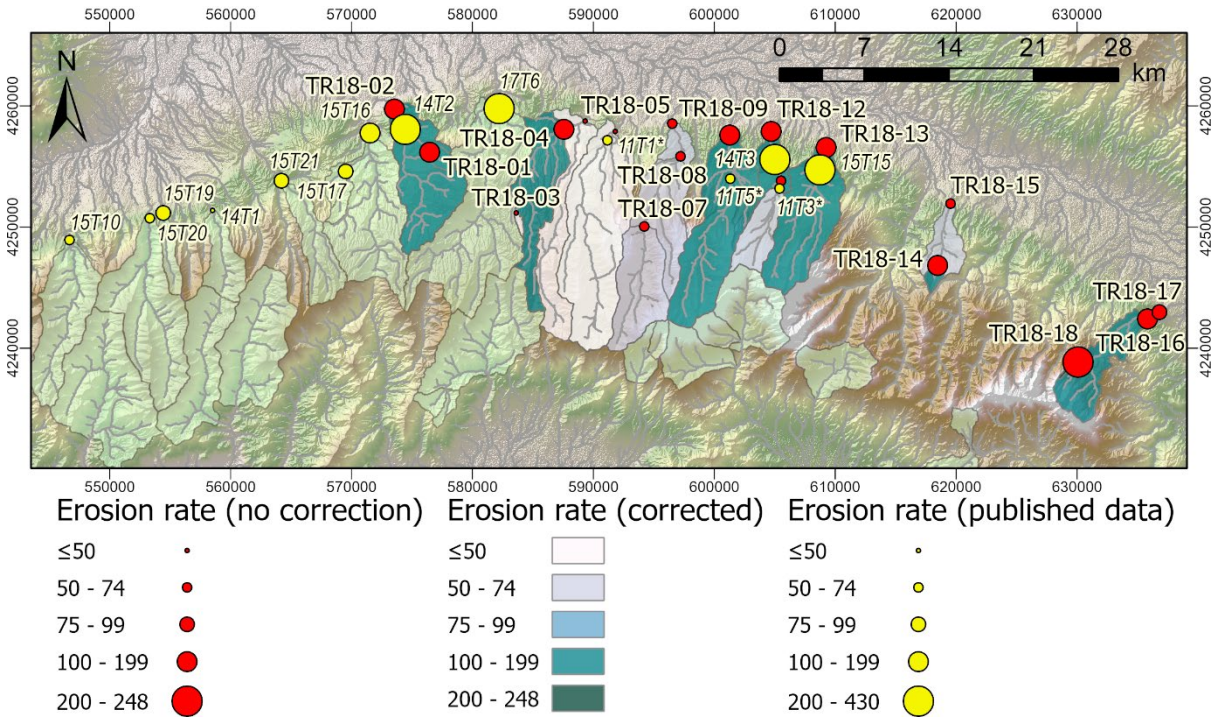


*Figure 7. Map of showing the catchment-averaged erosion rates along the Gediz Graben Boundary Fault. Yellow circles show previously published data (Buscher et al., 2013; Heineke et al., 2019); while red circles show rates derived here but without correction for sediment storage and recycling. Rates corrected for these factors are shown by the shading of the catchment areas.*

Interestingly, there are also differences in the CAER along individual sampled river systems with both decreasing and increasing erosion rates downstream being present (Figure 7). For example, and as expected, CAER increases along the Kabazlı River from 59 $mMyr^{-1}$ upstream of the Gediz Detachment fault to 157 $mMyr^{-1}$ at the boundary fault (Figure 7). By contrast, along the Badınca River (samples TR18-16 to TR18-18; easternmost river), burial-corrected erosion rates decrease downstream from ~ 250 $mMyr^{-1}$ in the headwaters to 86 $mMyr^{-1}$ upstream of the boundary fault. These data suggest that CAER do not scale simply with tectonic rates (c.f. Roda-Boluda et al., 2019) and may be influenced by factors such as sediment storage and contrasts in bedrock erodibility, which we evaluate below.

Secondly, the different CAER can also be compared with a range of topographic metrics that have previously been shown to correlate positively with erosion rates in previous studies such as relief and slope (i.e., Abbühl et al., 2011; Miller et al., 2013; Bellin et al., 2014; Kober et al., 2015). However, when the burial-corrected mixed rates (but not unmixed for low erosion rate areas) and published CAER data are plotted against mean catchment slope, topographic relief (150 m radius) and maximum incision depth upstream of the sample site there are no trends (Supplemental Figure 1).

By contrast, when these erosion rates are compared to the maximum upstream unit stream power there is a significant ($P< 0.05$) positive linear trend with erosion rate in the published data from Heineke et al., (2019)(Figure 8A; $r^2 = 0.8$). There are also significant ($P< 0.05$) positive linear ($r^2= 0.6 - 0.9$) relationships between erosion rates and steepness index for the published data of Buscher et al. (2013) and Hieneke et al. (2019)(Figure 8B) and a weak but significant linear relationship between erosion rates and throw rate on the graben boundary fault (figure 8C; $r^2= 0.2$). It is also noticeable that CAER expressed as m/Ma are lower than the slip rates on the basin bounding fault, particularly towards the centre of the fault, where displacement rates are 2 mm/yr (i.e. 2000 m/Ma) (Figure 6B).

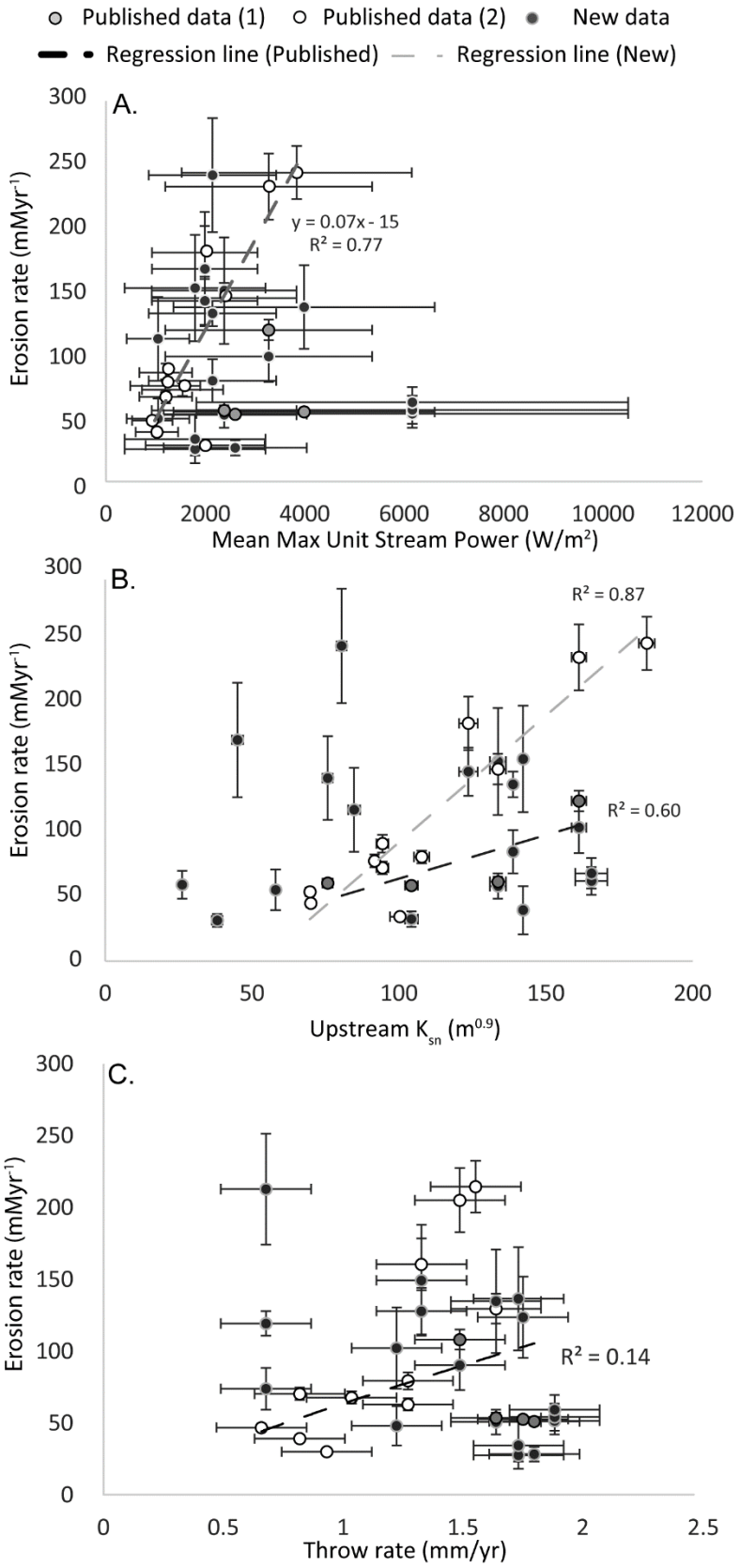


*Figure 8. Comparison of geomorphic variables A) mean maximum unit stream power and B) normalised steepness index upstream, and C) throw rate on the Gediz Graben Boundary Fault against catchment-averaged erosion rates for previously published data (1: Buscher et al., 2013; 2: Heineke et al., 2019) with internal uncertainty and for all samples collected here corrected for burial and sediment storage with calculated errors but not unmixed further.*

628

629 Thirdly, the unmixed CAER that represent erosion rates only in the transient reach
630 of the rivers can be compared with the same metrics. When these rates (which

include published data as well as the new data determined here) are plotted against mean catchment slope, topographic relief and maximum incision depth upstream of the sample location, again there are no clear or significant trends (Supplemental Figure 2). However, when unmixed CAER are compared to the upstream maximum unit stream power there is a broad positive trend but with only a very weak correlation (Figure 9A). Although when the Bozdağ samples are removed as potential outliers, because this river has very high stream power yet low erosion rates in the centre of the fault, a significant ($P < 0.05$) linear regression line with an $r^2 = 0.25$ can be plotted. Similarly, there is no trend between Ksn and CAER, but if the Gumusi cay sample is excluded as an outlier, there is weak ($r^2 = 0.2$) but significant ($P < 0.05$) positive relationship between erosion rates and steepness index with the best fit regression being an exponential trend (Figure 9B). When all unmixed CAERs are plotted against fault throw rate there is no trend; however, when the samples from the detachment are removed so that only samples close to or at the boundary fault are retained there is a weak ($r^2 = 0.1$) but not significant ($P > 0.05$) positive power law relationship between these two variables (Figure 9C).

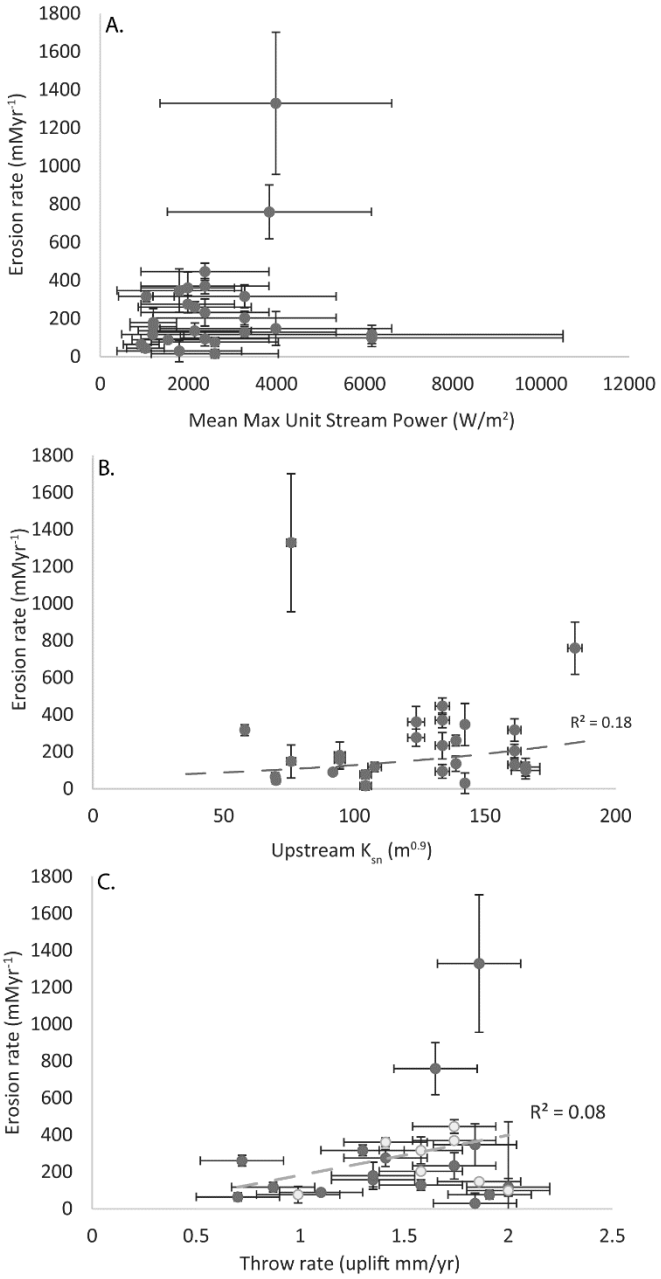


*Figure 9. Comparison of geomorphic variables A) maximum stream power and B) upstream steepness index, and C) throw rate on the Gediz Graben Boundary Fault against catchment-averaged erosion rate for previously published data and for samples collected here unmixed to remove the effect of the low erosion rate areas above the knickpoint. On C data have been separated into samples at the range front (dark) and at the detachment fault (light) to investigate the potential difference in erosion rates depending on the bedrock lithology.*

671

672 ### *4.4. Relationship between rock strength, geomorphology and*
673 ### *erosion rates*

674 In order to assess the impact that the different bedrock lithologies have on the
675 geomorphic response in the study region, the erosion rates for the different
676 catchments can be compared to measurements of bedrock strength. The bedrock
677 of the Bozdağ range can be broadly divided into the metamorphic lithologies of
678 the Menderes Massif and the unconformably overlying Miocene and younger
679 sediments. The metamorphic rocks are primarily composed of moderately strong
680 to strong (c.f., Selby, 1980) schists, gneisses and granites where the SRMS > 60

(Figure 10A) (c.f. Kent et al., 2021). By contrast, the syn-tectonic sandstones and conglomerates are weak to very weak (SRMS < 50). Therefore, if rock strength is the main control on CAER then the harder metamorphic rocks should be eroding at a lower rate than the softer sediments.

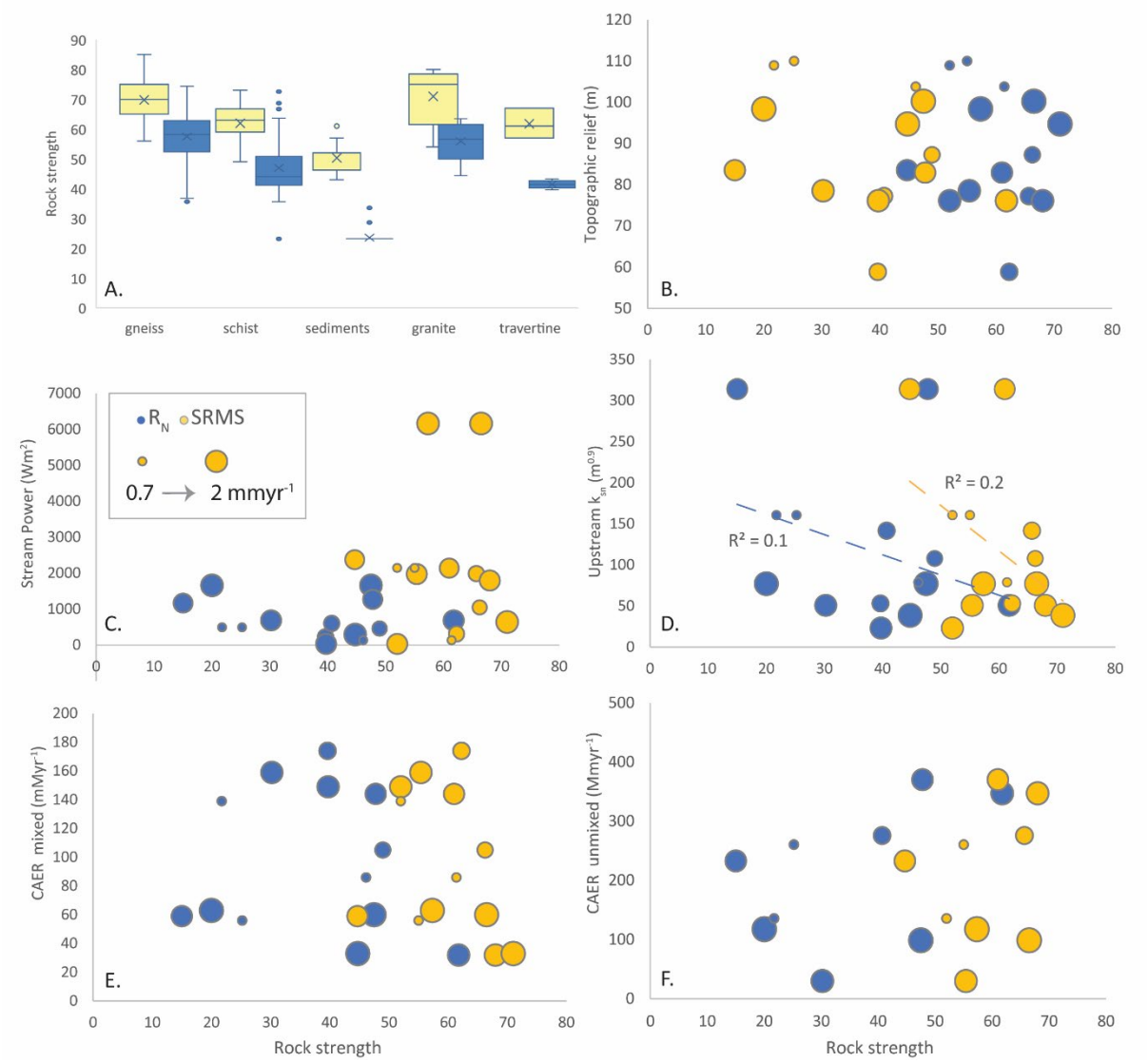


*Figure 10. A) Total Schmidt hammer rebound and SRMS for the main lithologies present in the study area. Schmidt hammer and SRMS calculated over 2 km upstream of the sample locations on the six main study rivers plotted against: B) topographic relief; C) maximum stream power; D) upstream normalised steepness index; E) catchment-averaged burial corrected erosion rates , and F) unmixed erosion rates for the transient reach of the rivers. On B-E the size of the circle proportionally represents the throw rate at the range front where the largest circles equal 2 mm/yr.*

Across the study region the strong metamorphic rocks are located south of the Gediz Detachment in the upland regions of the Bozdağ range, while the weak sedimentary rocks are mainly to the north, i.e., a soft over hard transition as represented in many landscape evolution models (e.g., Forte et al., 2016). Interestingly though when both measures of rock strength upstream of sample locations are compared to geomorphic variables such as relief (Figure 10B) and stream power (Figure 10C) there are no trends between the variables. This suggests that rock strength alone does not control relief or stream power. By contrast, there is a weak ($r^2 \leq 0.2$) negative linear relationship between rock strength (SRMS and Schmidt hammer rebound) and the upstream steepness index suggesting that rivers are on average less steep when the rocks are harder. However, this is not significant for either RMS or Schmidht Hammer rebound ($p > 0.05$) and is the opposite of the relationship that we would expect where the river is steeper in harder rocks. Furthermore, when CAERs are compared to the upstream rock strength, there is no clear relationship either for mixed or unmixed rates with both strong and weak rocks resulting in a similar range of CAERs (Figures 10 E and F). Finally, there are no clear trends of these variables with uplift rate on the fault as indicated by the size of the symbols on figures 10B-F.

# 5. Discussion

## *5.1. What controls erosion rates along the margin of the Gediz Graben?*

The geomorphology of the Bozdağ Range is shaped by the uplift along the Gediz Boundary fault and concomitant incision of the bedrock rivers resulting from the linkage of the boundary faults at ~ 0.8 Ma (Kent et al., 2017). Therefore, it is expected that there should be scaling relationships between various landscape metrics, uplift and erosion, similar to other regions around the world. For example, many studies show a positive relationship between CAER and catchment slope (i.e., Bellin et al., 2014; Rossi et al., 2017; Rosenkranz et al., 2018; Roda-Boluda et al., 2019) as well as positive relationship with channel steepness (Harkins et al., 2007; Cyr et al., 2010; DiBiase et al., 2010; Miller et al. 2013; Bellin et al., 2014; Rossi et al., 2017), which has been shown to be linear at low rates and steepness but becoming non-linear above a threshold steepness index. Related to landscape steepness is relief, which can either be measured as topographic relief

across the catchment, or following Roda-Boluda et al. (2018) as maximum incision depth (i.e., maximum local relief) along the river. In both measures, CAER have previously been shown to have a positive relationship with these factors. For example, Bellin et al. (2014) demonstrated a positive linear relationship with relief and Roda-Boluda et al. (2018) a positive power law relationship with maximum incision depth. This is not unexpected assuming little pre-existing topography, as areas of higher relief will have had more material eroded than areas of lower relief over the same time span, thus erosion rates should be higher where relief is higher. Though it is important to note that in general hillslopes have longer response times than rivers to changes in base-level (Simpson and Schlunegger, 2003; Schlunegger et al., 2013).

Unexpectedly, these trends appear not to hold true along the Bozdağ range either locally or catchment-wide, with no strong trends between erosion rates and average catchment slope, catchment relief or incision depth in either burial corrected CAER or unmixed for just the transient reach. While there are weak positive relationships observed in the data between CAER and normalised steepness index in the channel upstream of the sample point, this varies between a linear relationship for the whole CAER (not significant) and a weak but significant exponential for the transient reach only. The strongest and most significant of these weak trends is the linear relationship between the stream power and CAER (both burial-corrected and unmixed) albeit with larger uncertainites on the stream power data. These last two observations indicate that at the catchment scale and at the precision of our data, the rivers are broadly in line with a simple form of the stream power law, which is linear and n = 1 (Whipple and Tucker, 1999) where $E \approx KA^mS^n$ and is consistent with the analyses of Kent et al. (2021).

When CAER are compared to throw rates it is striking that erosion rates are around an order of magnitude lower than uplift rate. Given the presence of knickpoints and a documented transient landscape response (Kent et al., 2021, 2017) demonstrating that this region is not in topographic steady state, this relationship is to be expected. As a result the Bozdağ region will be experiencing surface uplift (Figures 8C and 9C). Yet, there are only weak positive relationships between the throw rate and CAERs, when corrected for sediment storage and for the presence of low relief zones. Additionally, it is striking that these relationships are only significant for the burial-corrected CAERs not for the unmixed CAERs. However,

762 this apparent contradiction is consistent with the documented fault linkage. After
763 a fault linkage event, the highest erosion rates should be present in the linkage
764 zones where the previous minimum in fault throw (as these were the tips of
765 individual faults) have had to rapidly increase to achieve the ideal fault profile
766 (Kent et al., 2016), higher uplift rates will also result in increased erosion in these
767 zones. This will also result in the part of the fault with the highest slip rates
768 experiencing lower erosion rates and as a result in the transient reaches throw
769 rate will not scale with erosion rate. Interestingly, at a catchment level the CAERs
770 do scale with throw rate but the correlation is weak perhaps suggesting that prior
771 to fault linkage throw rate did correlate with erosion rate.

772 A number of factors may cause the scatter and the weak correlations in these
773 data, which we explore below. One complication to consider is that the results
774 could be affected by sediment storage or non-uniform erosion as a result of
775 landsliding (e.g., Binnie et al., 2006; Kober et al., 2012; Roda-Boluda et al., 2018).
776 Neither of these factors appear to be likely along the Bozdağ range as firstly, the
777 potential effect of sediment storage has been corrected through the inclusion of
778 $^{26}$Al CRN data. Secondly, there is little evidence for significant landsliding in the
779 study region to deliver material with sufficiently low $^{10}$Be concentrations to perturb
780 the measured river sediment concentrations. Incomplete sediment mixing could
781 also explain the scatter in the data, while the measured CRN concentrations of
782 repeat samples along several river systems are within 2σ error, we have limited
783 data across the entire range to fully assess this issue, which has been shown to
784 be a complicating factor in mountainous catchments elsewhere (Binnie et al.,
785 2006).

786 Alternatively, the presence of inherited topography may play a significant role in
787 the landscape response to uplift (c.f., Densmore et al., 2009). This explanation is
788 supported by the clear imprint of the fault segments in the topographic metrics
789 and the observation that in the eastern part of the range higher slopes and relief
790 are found upstream of the tectonic knickpoint (Figure 6), despite transient river
791 incision downstream of the knickpoint. Therefore, inherited topography might
792 explain the disconnect between erosion rates and catchment wide variables such
793 as slope and relief and potentially the variability in the CAER derived from the five
794 samples taken from at or above the knickpoint. Yet if this explanation was the
795 only confounding factor, the unmixed CAER data should show stronger correlations

with stream power and steepness index in particular, as the effect of low relief/low erosion rate zones have been accounted for in this calculation, and burial-corrected CAER for the whole catchments might be expected to show relationships with catchment mean slope or relief, which they do not. Therefore, another explanation for the spread in the data could be the influence of a strong lithological contrast within the catchments, which is discussed further below.

### *5.2. The role of rock strength and lithology*

A number of recent models have explored the impact of lithological variability on river evolution and erosion rates that could be used to understand the relationships between CAER and the topographic metrics. Forte et al.'s (2016) model of using two distinct lithologies is highly applicable to the Gediz Graben. Their work demonstrated that when soft rocks overlie hard rocks along downstream dipping contact, the lithological contact becomes an important and persistent topographic feature in the landscape with the contact's dip-slope being preserved. This can clearly be seen in the study area as the Gediz Detachment is a pervasive feature along much of the range, and in many interfluve areas the detachment is well preserved with little evidence of deep erosion.

Indeed, the presence of a very strong but thin cataclasite band found along the low-angle Gediz Detachment was used by Heineke et al. (2019) to explain the presence of low erosion rates and gentle slopes. In addition, they proposed that 'weak' phyllites and schists result in higher erosion rates in the centre of the range. The results presented here do not support this latter point, as lower CAERs are found in the centre of the range (Figure 7) and figures 10E and F show the CAER are invariant with rock strength upstream of the sample location despite a two-fold difference in strength between the sedimentary and metamorphic rocks overall (Figure 10A) and associated differences in erodibilty (Kent et al., 2021). This contradiction speaks to the difficulty in accurately constraining rock strength and erodibility in the field, determining the best categorisation, and linking such data to observed changes in fluvial behaviour and erosion rates (e.g., Bursztyn et al., 2015; Zondervan et al., 2020).

In addition, Forte et al.'s (2016) landscape evolution model also suggests that although the lithological boundary moves downstream over time, the erosion rates

above and below the boundary will diverge. The soft rocks downstream will erode at the imposed uplift rate while the underlying hard rocks erode at a rate lower than the regional uplift rate. Another implication of Forte et al.'s (2016) landscape evolution model is that CAER would be perturbed or amplified downstream as a result of the lithological variation. We see that erosion rates of the underlying hard metamorphic rocks are eroding at rates lower than inferred uplift rates (Figure 9C), consistent with the landscape evolution model outputs. However, the erosion rates in the sedimentary bedrock reaches are also much lower than uplift rates at the graben boundary fault (Figure 9C), and only weakly and not significantly scale with throw rates on the fault.

Interestingly, Kent et al. (2021) demonstrated that stream power scales with uplift rate in the metamorphic bedrock reaches of their six study rivers. But uplift does not scale with stream power in the sedimentary reaches where sediment transport appears to be more important, resulting in a difference in the fluvial response in these reaches owing to the abundance of sedimentary material entering the river system (Kent et al., 2021). Therefore, while erosion rates in the sedimentary reaches still weakly scale with the uplift rate the influence of sediment transport and hybrid or transport-limited nature of these lower reaches causes the erosion rate to be lower. In this study area the lithological control on landscape evolution is therefore manifested not as bedrock erodibility but in variable fluvial responses that are not captured in a detachment-limited landscape evolution model. A key challenge for the future is to understand how the spatially variable erosion rates captured here are integrated over time to produce a coherent relief and sediment flux signal.

## 6. Conclusions

Eighteen samples were collected for $^{10}$Be and $^{26}$Al cosmogenic nuclide analysis and combined with a further 15 previously published $^{10}$Be concentrations (Buscher et al., 2013; Heineke et al., 2019) to determine catchment-averaged erosion rates along strike of the well-constrained Gediz Fault system in western Türkiye. This area features a significant lithological contrast where soft sediments overlie hard metamorphic rocks along a moderately dipping downstream contact, a series of north-flowing rivers are incising through this contact as a result of uplift along the

fault at rates of up 2 mmyr$^{-1}$ and a fault-linkage event at ~0.8 Ma (Kent et al., 2017). This natural laboratory allows the results of recent landscape evolution models investigating the role of such lithological contrasts to be tested. The background rate of erosion of the pre-incision landscape is determined as 46 ± 46 mMyr$^{-1}$ and erosion rates within the transient reach vary from 16 – 1330 mMyr$^{-1}$. Although, erosion rates weakly scale with unit stream power, steepness index and slip rate on the bounding fault, there are no clear relationships between erosion rate and relief or catchment slope. Catchment-wide and within the transient reach erosion rates are an order of magnitude lower than slip rates for both metamorphic and sedimentary reaches and despite a 30-fold difference in erodibility there is no difference in the erosion rate between strong and weak rocks. This finding is at odds with the results of landscape evolution modelling and is likely owing to the influence of sediment transport on fluvial dynamics in the sedimentary reaches, i.e., some rivers are not completely detachment-limited. While the weak relationships between other variables remain unexplained but maybe the result of incomplete sediment mixing or the influence of pre-existing topography prior to the onset of the current incisional phase. These findings indicate that the erosional response to uplift along an active normal fault is a complex response to multiple drivers that vary spatially and temporally.

## Acknowledgements

We acknowledge a NERC Facilities grant (CIAF/9189/1018) for the cosmogenic analysis and a Geological Society field work grant both awarded to S.J.Boulton that supported this research. The code used to calculate the burial corrected erosion rates using both $^{10}$Be and $^{26}$Al can be found at: https://github.com/angelrodes/banana1026. Figure 5 was plotted using CosmoCalc (Vermeesch, 2007) available for download from https://www.ucl.ac.uk/~ucfbpve/cosmocalc/

## References

Abbühl, L.M., Norton, K.P., Jansen, J.D., Schlunegger, F., Aldahan, A., Possnert, G., 2011. Erosion rates and mechanisms of knickzone retreat inferred from

10Be measured across strong climate gradients on the northern and central Andes Western Escarpment. Earth Surf. Process. Landforms 36, 1464–1473. https://doi.org/10.1002/esp.2

Adams, B.A., Whipple, K.X., Forte, A.M., Heimsath, A.M. and Hodges, K.V., 2020. Climate controls on erosion in tectonically active landscapes. Science Advances, 6(42), p.eaaz3166.164

Attal, M., Cowie, P. a., Whittaker, a. C., Hobley, D., Tucker, G.E., Roberts, G.P., 2011. Testing fluvial erosion models using the transient response of bedrock rivers to tectonic forcing in the Apennines, Italy. J. Geophys. Res. Earth Surf. 116, 1–17. https://doi.org/10.1029/2010JF001875

Balco, G., Stone, J.O., Lifton, N.A., Dunai, T.J., 2008. A complete and easily accessible means of calculating surface exposure ages or erosion rates from 10Be and 26Al measurements. Quat. Geochronol. https://doi.org/10.1016/j.quageo.2007.12.001

Bellin, N., Vanacker, V., Kubik, P.W., 2014. Denudation rates and tectonic geomorphology of the Spanish Betic Cordillera. Earth Planet. Sci. Lett. 390, 19–30. https://doi.org/10.1016/J.EPSL.2013.12.045

Bellin, N, Vanacker, V., Kubik, P.W., 2014. Denudation rates and tectonic geomorphology of the Spanish Betic Cordillera. Earth Planet. Sci. Lett. 390, 19–30. https://doi.org/10.1016/j.epsl.2013.12.045

Bernard, T., Sinclair, H.D., Gailleton, B., Mudd, S.M., Ford, M., 2019. Lithological control on the post-orogenic topography and erosion history of the Pyrenees. Earth Planet. Sci. Lett. 518, 53–66. https://doi.org/10.1016/J.EPSL.2019.04.034

Binnie, S.A., Phillips, W.M., Summerfield, M.A., Fifield, L.K., 2006. Sediment mixing and basin-wide cosmogenic nuclide analysis in rapidly eroding mountainous environments. Quat. Geochronol. 1, 4–14.

Boulton, S.J., Stokes, M., 2018. Which DEM is best for analyzing fluvial landscape development in mountainous terrains? Geomorphology 310. https://doi.org/10.1016/j.geomorph.2018.03.002

Burdis, A.J., 2014. Denudation rates derived from spatially-averaged cosmogenic

925 nuclide analysis in Nelson/Tasman catchments, South Island, New Zealand.

926 Bursztyn, N., Pederson, J.L., Tressler, C., Mackley, R.D., Mitchell, K.J., 2015.
927 Rock strength along a fluvial transect of the Colorado Plateau–quantifying a
928 fundamental control on geomorphology. Earth Planet. Sci. Lett. 429, 90–
929 100.

930 Buscher, J.T., Hampel, A., Hetzel, R., Dunkl, I., Glotzbach, C., Struffert, A., Akal,
931 C., Rätz, M., 2013. Quantifying rates of detachment faulting and erosion in
932 the central Menderes Massif (western Turkey) by thermochronology and
933 cosmogenic 10 Be. J. Geol. Soc. London. 170, 669–683.
934 https://doi.org/10.1144/jgs2012-132

935 Child, D., Elliott, G., Mifsud, C., Smith, A.M., Fink, D., 2000. Sample processing
936 for earth science studies at ANTARES. Nucl. Instruments Methods Phys. Res.
937 Sect. B Beam Interact. with Mater. Atoms 172, 856–860.

938 Cyr, A.J., Granger, D.E., Olivetti, V., Molin, P., 2010. Quantifying rock uplift
939 rates using channel steepness and cosmogenic nuclide–determined erosion
940 rates: Examples from northern and southern Italy. Lithosphere 2, 188–198.
941 https://doi.org/10.1130/L96.1

942 D'Arcy, M., Whittaker, A.C., 2014. Geomorphic constraints on landscape
943 sensitivity to climate in tectonically active areas. Geomorphology 204, 366–
944 381. https://doi.org/10.1016/j.geomorph.2013.08.019

945 Darling, A., Whipple, K., Bierman, P., Clarke, B., Heimsath, A., 2020. Resistant
946 rock layers amplify cosmogenically-determined erosion rates. Earth Surf.
947 Process. Landforms 45, 312–330.
948 https://doi.org/https://doi.org/10.1002/esp.4730

949 Densmore, A.L., Hetzel, R., Ivy-Ochs, S., Krugh, W.C., Dawers, N., Kubik, P.,
950 2009. Spatial variations in catchment-averaged denudation rates from
951 normal fault footwalls. Geology 37, 1139–1142.
952 https://doi.org/10.1130/G30164A.1

953 DiBiase, R.A., Whipple, K.X., Heimsath, A.M., Ouimet, W.B., 2010. Landscape
954 form and millennial erosion rates in the San Gabriel Mountains, CA. Earth
955 Planet. Sci. Lett. 289, 134–144.

https://doi.org/10.1016/J.EPSL.2009.10.036

Dingle, H.E., Sinclair, D.H., Attal, M., Rodés, A., Singh, V., 2018. Temporal variability in detrital 10Be concentrations in a large Himalayan catchment. Earth Surf. Dyn. 6, 611–635. https://doi.org/10.5194/esurf-6-611-2018

Finnegan, N.J., Roe, G., Montgomery, D.R., Hallet, B., 2005. Controls on the channel width of rivers: Implications for modeling fluvial incision of bedrock. Geology 33, 229–232. https://doi.org/10.1130/G21171.1

Forte, A.M., Whipple, K.X., 2018. Criteria and tools for determining drainage divide stability. Earth Planet. Sci. Lett. 493, 102–117. https://doi.org/10.1016/J.EPSL.2018.04.026

Forte, A.M., Yanites, B.J., Whipple, K.X., 2016. Complexities of landscape evolution during incision through layered stratigraphy with contrasts in rock strength. Earth Surf. Process. Landforms 41, 1736–1757. https://doi.org/10.1002/esp.3947

Gailleton, B., Sinclair, H. D., Mudd, S. M., Graf, E. L. S., & Maţenco, L. C. (2021). Isolating lithologic versus tectonic signals of river profiles to test orogenic models for the Eastern and Southeastern Carpathians. Journal of Geophysical Research: Earth Surface, 126, e2020JF005970.

Glodny, J., Hetzel, R., 2007. Precise U–Pb ages of syn-extensional Miocene intrusions in the central Menderes Massif, western Turkey. Geol. Mag. 144, 235–246. https://doi.org/DOI: 10.1017/S0016756806003025

Goudie, A.S., 2016. Quantification of rock control in geomorphology. Earth-Science Rev. 159, 374–387. https://doi.org/10.1016/J.EARSCIREV.2016.06.012

Granger, D., Kirchner, J., Finkel, R., 1996. Spatially Averaged Long-Term Erosion Rates Measured From In Situ-Produced Cosmogenic Nuclides in Alluvial Sediment. J. Geol. 104, 249–257. https://doi.org/10.1086/629823

Granger, D.E., Muzikar, P.F., 2001. Dating sediment burial with in situ-produced cosmogenic nuclides: theory, techniques, and limitations. Earth Planet. Sci. Lett. 188, 269–281.

Harel, M.A., Mudd, S.M., Attal, M., 2016. Global analysis of the stream power

law parameters based on worldwide 10Be denudation rates. Geomorphology. https://doi.org/10.1016/j.geomorph.2016.05.035

Harkins, N., Kirby, E., Heimsath, A., Robinson, R., Reiser, U., 2007. Transient fluvial incision in the headwaters of the Yellow River, northeastern Tibet, China. J. Geophys. Res. Earth Surf. 112, 1–21. https://doi.org/10.1029/2006JF000570

Heineke, C., Hetzel, R., Nilius, N.-P., Glotzbach, C., Akal, C., Christl, M., Hampel, A., 2019. Spatial patterns of erosion and landscape evolution in a bivergent metamorphic core complex revealed by cosmogenic 10Be: The central Menderes Massif (western Turkey). Geosphere 15, 1846–1868. https://doi.org/10.1130/GES02013.1

Kent, E., Boulton, S.J., Whittaker, A.C., Stewart, I.S., Cihat Alçiçek, M., 2017. Normal fault growth and linkage in the Gediz (Alaşehir) Graben, Western Turkey, revealed by transient river long-profiles and slope-break knickpoints. Earth Surf. Process. Landforms 42. https://doi.org/10.1002/esp.4049

Kent, E., Whittaker, A.C., Boulton, S.J., Alçiçek, M.C., 2021. Quantifying the competing influences of lithology and throw rate on bedrock river incision. GSA Bull. 133, 1649–1664. https://doi.org/10.1130/B35783.1

Kent, E.J., 2015. The relationship between active faulting and fluvial geomorphology: a case study in the Gediz Graben, Turkey.PhD Thesis; University of Plymouth, 397 pp.

Kirby, E., Whipple, K.X., 2012. Expression of active tectonics in erosional landscapes. J. Struct. Geol. 44, 54–75. https://doi.org/10.1016/j.jsg.2012.07.009

Kober, F., Hippe, K., Salcher, B., Ivy-Ochs, S., Kubik, P.W., Wacker, L., Hählen, N., 2012. Debris-flow–dependent variation of cosmogenically derived catchment-wide denudation rates. Geology 40, 935–938.

Kober, F., Zeilinger, G., Hippe, K., Marc, O., Lendzioch, T., Grischott, R., Christl, M., Kubik, P.W., Zola, R., 2015. Tectonic and lithological controls on denudation rates in the central Bolivian Andes. Tectonophysics 657, 230–

244. https://doi.org/10.1016/j.tecto.2015.06.037

Lal, D., 1991. Cosmic ray labeling of erosion surfaces: in situ nuclide production rates and erosion models. Earth and Planetary Science Letters, 104(2-4), 424-439.

Miller, S. R., Sak, P. B., Kirby, E., Bierman, P.R., 2013. Neogene rejuvenation of central Appalachian topography: Evidence for differential rock uplift from stream profiles and erosion rates. Earth Planet. Sci. Lett. 369–370, 1–12. https://doi.org/10.1016/J.EPSL.2013.04.007

Miller, S.R., Baldwin, S.L., Fitzgerald, P.G., 2012. Transient fluvial incision and active surface uplift in the Woodlark Rift of eastern Papua New Guinea. Lithosphere 4, 131–149. https://doi.org/10.1130/L135.1

Mitchell, N.A., Yanites, B.J., 2021. Bedrock river erosion through dipping layered rocks: quantifying erodibility through kinematic wave speed. Earth Surf. Dyn. 9, 723–753. https://doi.org/10.5194/esurf-9-723-2021

Ortega, J. a., Wohl, E., Livers, B., 2013. Waterfalls on the eastern side of Rocky Mountain National Park, Colorado, USA. Geomorphology 198, 37–44. https://doi.org/10.1016/j.geomorph.2013.05.010

Ouimet, W.B., Whipple, K.X., Granger, D.E., 2009. Beyond threshold hillslopes: Channel adjustment to base-level fall in tectonically active mountain ranges. Geology 37, 579–582. https://doi.org/10.1130/G30013A.1

Peifer, D., Persano, C., Hurst, M. D., Bishop, P., & Fabel, D. (2020). Growing topography due to contrasting rock types in a tectonically dead landscape. Earth Surface Dynamics, 2021, 167-181. https://doi.org/10.5194/esurf-9-167-2021

Perne, M., Covington, M.D., Thaler, E.A., Myre, J.M., 2017. Steady state, erosional continuity, and the topography of landscapes developed in layered rocks. Earth Surf. Dyn. 5. https://doi.org/10.5194/esurf-5-85-2017

Regalla, C., Kirby, E., Fisher, D., Bierman, P., 2013. Active forearc shortening in Tohoku, Japan: Constraints on fault geometry from erosion rates and fluvial longitudinal profiles. Geomorphology 195, 84–98. https://doi.org/10.1016/j.geomorph.2013.04.029

Roda-Boluda, D.C., D'Arcy, M., Whittaker, A.C., Gheorghiu, D.M., Rodés, Á., 2019. 10Be erosion rates controlled by transient response to normal faulting through incision and landsliding. Earth Planet. Sci. Lett. 507, 140–153. https://doi.org/10.1016/j.epsl.2018.11.032

Roda-Boluda, D.C., D'Arcy, M., McDonald, J., Whittaker, A.C., 2018. Lithological controls on hillslope sediment supply: insights from landslide activity and grain size distributions. Earth Surf. Process. Landforms 43, 956–977.

Rodés, Á., 2021. The NUNAtak Ice Thinning (NUNAIT) calculator for cosmonuclide elevation profiles. Geosciences 11, 362.

Rosenkranz, R., Schildgen, T., Wittmann, H., Spiegel, C., 2018. Coupling erosion and topographic development in the rainiest place on Earth: Reconstructing the Shillong Plateau uplift history with in-situ cosmogenic 10Be. Earth Planet. Sci. Lett. 483, 39–51. https://doi.org/10.1016/j.epsl.2017.11.047

Rossi, M.W., Quigley, M.C., Fletcher, J.M., Whipple, K.X., Díaz-Torres, J.J., Seiler, C., Fifield, L.K., Heimsath, A.M., 2017. Along-strike variation in catchment morphology and cosmogenic denudation rates reveal the pattern and history of footwall uplift, Main Gulf Escarpment, Baja California. Bull. Geol. Soc. Am. 129, 837–854. https://doi.org/10.1130/B31373.1

Safran, E.B., Bierman, P.R., Aalto, R., Dunne, T., Whipple, K.X., Caffee, M., 2005. Erosion rates driven by channel network incision in the Bolivian Andes. Earth Surf. Process. Landforms J. Br. Geomorphol. Res. Gr. 30, 1007–1024.

Schlunegger, F., Norton, K., Caduff, R. and Shroder, J.F., 2013. Hillslope processes in temperate environments. Treatise in Geomorphology, 3, pp.337-354.

Schwanghart, W., Scherler, D., 2014. TopoToolbox 2 – MATLAB-based software for topographic analysis and modeling in Earth surface sciences. Earth Surf. Dyn. 2. https://doi.org/10.5194/esurf-2-1-2014]

Selby, M.J., 1980. A rock mass strength classification for geomorphic purposes: with tests from Antarctica and New Zealand. Zeitschrift für Geomorphol. 31–51.

Simpson, G., and F. Schlunegger, 2003. Topographic evolution and morphology of surfaces evolving in response to coupled fluvial and hillslope sediment transport, J. Geophys. Res., 108(B6), 2300, doi:10.1029/2002JB00216.

Sklar, L.S., Dietrich, W.E., 2001. Sediment and rock strength controls on river incision into bedrock. Geology 29, 1087–1090. https://doi.org/10.1130/0091-7613

Snyder, N.P., Whipple, K.X., Tucker, G.E., Merritts, D.J., 2000. Stream profiles in the Mendocino triple junction region, northern California. GSA Bull. 112, 1250–1263. https://doi.org/10.1130/0016-7606

Stolle, A., Schwanghart, W., Andermann, C., Bernhardt, A., Fort, M., Jansen, J.D., Wittmann, H., Merchel, S., Rugel, G., Adhikari, B.R., Korup, O., 2019. Protracted river response to medieval earthquakes. Earth Surface Processes and Landforms, 44, 331-341.

Sullivan, D.G., 1988. The discovery of Santorini Minoan tephra in western Turkey. Nature 333, 552–554. https://doi.org/10.1038/333552a0

Süzen, M.L., Toprak, V., Rojay, B., 2006. High-altitude Plio–Quaternary fluvial deposits and their implication on the tilt of a horst, western Anatolia, Turkey. Geomorphology 74, 80–99. https://doi.org/10.1016/J.GEOMORPH.2005.07.012

Vermeesch, P., 2007. CosmoCalc: An Excel add-in for cosmogenic nuclide calculations. Geochemistry, Geophysics, Geosystems, 8(8).

Whipple, K.X., Tucker, G.E., 1999. Dynamics of the stream-power river incision model: Implications for height limits of mountain ranges, landscape response timescales, and research needs. J. Geophys. Res. Solid Earth 104, 17661–17674. https://doi.org/10.1029/1999JB900120

Whittaker, A.C., 2012. How do landscapes record tectonics and climate? Lithosphere 4. https://doi.org/10.1130/RF.L003.1

Whittaker, A.C., Boulton, S.J., 2012. Tectonic and climatic controls on knickpoint retreat rates and landscape response times. J. Geophys. Res. Earth Surf. 117.

Whittaker, A.C., Cowie, P. a., Attal, M., Tucker, G.E., Roberts, G.P., 2007.

Bedrock channel adjustment to tectonic forcing: Implications for predicting river incision rates. Geology 35, 103–106. https://doi.org/10.1130/G23106A.1

Wobus, C., Whipple, K.X., Kirby, E., Snyder, N., Johnson, J., Spyropolou, K., Crosby, B., Sheehan, D., 2006. Tectonics from topography: Procedures, promise, and pitfalls, in: Willett, S.D., Hovius, N., Brandon, M.T., Fisher, D.M. (Eds.), Tectonics, Climate, and Landscape Evolution. Geological Society of America, p. 0. https://doi.org/10.1130/2006.2398(04)

Wolpert, J.A., Forte, A.M., 2021. Response of transient rock uplift and base level knickpoints to erosional efficiency contrasts in bedrock streams. Earth Surf. Process. Landforms n/a. https://doi.org/https://doi.org/10.1002/esp.5146

Xu, S., Dougans, A.B., Freeman, S.P.H.T., Schnabel, C., Wilcken, K.M., 2010. Improved 10Be and 26Al-AMS with a 5 MV spectrometer. Nucl. Instruments Methods Phys. Res. Sect. B Beam Interact. with Mater. Atoms 268, 736–738.

Yanites B.J. Tucker G.E. Anderson R.S., 2009, Numerical and analytical models of cosmogenic radionuclide dynamics in landslide-dominated drainage basins: Journal of Geophysical Research , v. 114, F01007, doi:10.1029/2008jf001088

Zondervan, Jesse R, Stokes, M., Boulton, S.J., Telfer, M.W., Mather, A.E., 2020. Rock strength and structural controls on fluvial erodibility: Implications for drainage divide mobility in a collisional mountain belt. Earth Planet. Sci. Lett. 538, 116221. https://doi.org/https://doi.org/10.1016/j.epsl.2020.116221

Zondervan, Jesse R., Whittaker, A.C., Bell, R.E., Watkins, S.E., Brooke, S.A.S., Hann, M.G., 2020. New constraints on bedrock erodibility and landscape response times upstream of an active fault. Geomorphology 351, 106937. https://doi.org/10.1016/J.GEOMORPH.2019.106937